Bioactive Materials 43 (2025) 255–272

Contents lists available at ScienceDirect

Bioactive Materials

journal homepage: www.keaipublishing.com/en/journals/bioactive-materials

Self-assembled PROTACs enable protein degradation to reprogram the tumor microenvironment for synergistically enhanced colorectal cancer immunotherapy

Xinchen Lu [a,d,1], Jinmei Jin [a,1], Ye Wu [a,1], Jiayi Lin [a], Xiaokun Zhang [a], Shengxin Lu [a], Jiyuan Zhang [a,d], Chunling Zhang [a], Maomao Ren [a], Hongzhuan Chen [a,*], Weidong Zhang [a,b,c,d,**], Xin Luan [a,***]

[a] Shanghai Frontiers Science Center for Chinese Medicine Chemical Biology, Institute of Interdisciplinary Integrative Medicine Research and Shuguang Hospital, Shanghai University of Traditional Chinese Medicine, Shanghai, 201203, China
[b] State Key Laboratory for Quality Ensurance and Sustainable Use of Dao-di Herbs, Institute of Medicinal Plant Development, Chinese Academy of Medical Sciences & Peking Union Medical College, Beijing, 100700, China
[c] School of Pharmacy, Second Military Medical University, Shanghai, 200433, China
[d] School of Pharmacy, Fudan University, Shanghai, 201203, China

ARTICLE INFO

Keywords:
STAT3
β-catenin
NP-PROTACs
Immunosuppressive microenvironment
Colorectal cancer therapy

ABSTRACT

Both β-catenin and STAT3 drive colorectal cancer (CRC) growth, progression, and immune evasion, and their co-overexpression is strongly associated with a poor prognosis. However, current small molecule inhibitors have limited efficacy due to the reciprocal feedback activation between STAT3 and β-catenin. Inspired by the PROteolysis TArgeting Chimera (PROTAC), a promising pharmacological modality for the selective degradation of proteins, we developed a strategy of nanoengineered peptide PROTACs (NP-PROTACs) to degrade both β-catenin and STAT3 effectively. The NP-PROTACs were engineered by coupling the peptide PROTACs with DSPE-PEG via disulfide bonds and self-assembled into nanoparticles. Notably, the dual degradation of β-catenin and STAT3 mediated by NP-PROTACs led to a synergistic antitumor effect compared to single-target treatment. Moreover, NP-PROTACs treatment enhanced $CD103^{+}$ dendritic cell infiltration and T-cell cytotoxicity, alleviating the immunosuppressive microenvironment induced by β-catenin/STAT3 in CRC. These results highlight the potential of NP-PROTACs in facilitating the simultaneous degradation of two pathogenic proteins, thereby providing a novel avenue for cancer therapy.

1. Introduction

Colorectal cancer (CRC) currently ranks as the second most prevalent cancer worldwide in terms of both incidence and mortality [1]. Due to the high tumor heterogeneity and compensatory mechanisms in CRC, single-target treatment strategies frequently exhibit limited potency or are susceptible to the development of drug resistance [2]. Consequently, multitargeted combination therapy offers the prospects of enhanced efficacy, improved safety profiles, and a lower tendency to induce drug resistance for cancer treatment compared to monotherapy [3,4]. Various combination therapy strategies have been widely applied in clinical practice, such as combining immune checkpoint inhibitors with anti-EGFR agents and BRAF inhibitors with MEK inhibitors [5]. Therefore, elucidating more detailed molecular mechanisms and identifying effective therapeutic targets have important clinical significance for targeted therapy of CRC.

Peer review under responsibility of KeAi Communications Co., Ltd.
* Corresponding author.
** Corresponding author. Shanghai Frontiers Science Center for Chinese Medicine Chemical Biology, Institute of Interdisciplinary Integrative Medicine Research and Shuguang Hospital, Shanghai University of Traditional Chinese Medicine, Shanghai, 201203, China.
*** Corresponding author.
E-mail addresses: hongzhuan_chen@hotmail.com (H. Chen), wdzhangy@hotmail.com (W. Zhang), luanxin@shutcm.edu.cn (X. Luan).
[1] These authors contributed equally.

https://doi.org/10.1016/j.bioactmat.2024.09.022
Received 20 March 2024; Received in revised form 21 August 2024; Accepted 17 September 2024
2452-199X/© 2024 The Authors. Publishing services by Elsevier B.V. on behalf of KeAi Communications Co. Ltd. This is an open access article under the CC BY-NC-ND license (http://creativecommons.org/licenses/by-nc-nd/4.0/).

The Wnt/β-catenin and Janus kinase/signal transducer and activator of transcription (JAK/STAT) pathways are two crucial pathways that mediate the occurrence and progression of CRC [6,7]. Mutations in the former pathway and phosphorylation-mediated activation of the latter signaling pathway are observed in most CRC patients [8,9]. Among them, β-catenin and STAT3 emerge as pivotal transcription factors that orchestrate the expression of diverse oncogenic proteins [10,11], and β-catenin and STAT3 are commonly co-activated in CRC, with 92.5 % of CRC patients exhibiting positive nuclear β-catenin when phosphorylated STAT3 is present [12]. Significantly, the co-overexpression of β-catenin and STAT3 in CRC has been correlated with decreased patient survival rates and the establishment of a tumor immunosuppressive microenvironment (TIME) [13,14]. The upregulation of β-catenin levels hampers the expression of C-C motif chemokine ligand 4 (CCL4), thereby impeding the recruitment of $CD103^+$ dendritic cells (DCs) to tumor tissues and ultimately leading to a decrease in $CD8^+$ T-cell infiltration [15]. Moreover, our previous research has also revealed that STAT3 functions as a programmed cell death 1 ligand 1 (PD-L1) promoter, which mediates a crucial mechanism for inhibiting T-cell recognition and cytotoxicity against tumor cells [16]. Thus, simultaneous inhibition of both β-catenin and STAT3 at tumor sites is highly desirable and holds great potential for achieving synergistic CRC immunotherapy.

Despite the utilization of numerous small molecule inhibitors of β-catenin or STAT3 in preclinical studies, their clinical development still encounters obstacles such as low affinity and selectivity [17,18]. In addition, inhibitors targeting β-catenin or STAT3 face similar challenges: 1) As transcription factors, these two proteins lack binding pockets for small molecules. 2) Binding to a single domain of these two proteins may not wholly suppress their transcriptional activities (β-catenin contains TCF binding sites, BCL9 binding sites, and phosphorylation sites; STAT3 possesses phosphorylation sites and dimerization sites). 3) Due to the high sequence similarity between STAT3 and other STAT family members, the homology of β-catenin with CBP and p300, and complex protein-protein interaction between β-catenin and binding partners such as TCF and AXIN, small molecule inhibitors often exhibit poor selectivity, resulting in off-target toxicity. Thus, there is an urgent need to develop more effective targeting strategies for β-catenin- or STAT3-dependent CRC therapy.

The PROteolysis TArgeting Chimera (PROTAC) strategy exploits the ubiquitin-proteasome system to degrade “undruggable” targets through the target protein-PROTAC-E3 ubiquitin ligase complex [19,20]. Unlike traditional inhibitors, PROTACs do not need prolonged occupancy of the binding site to exert pharmacological activity, enabling efficacy with lower-affinity ligands [21,22]. Furthermore, PROTACs can simultaneously inhibit all activities of multifunctional proteins [23] through protein degradation [24]. However, despite being promising, current small-molecule-based PROTACs still suffer from poor water solubility, limited tissue selectivity, and inadequate tumor penetration for effective cancer treatment.

Compared with small molecules, peptides are more effective modulators of β-catenin [25] and STAT3 [26]. Peptide-based PROTACs have shown great promise for durably degrading β-catenin in CRC patient-derived tumor organoids [27]. However, two inherent pharmacological weaknesses limit the use of peptides as PROTACs: poor membrane permeability and low proteolytic stability. Nanomedicine plays a crucial role in cancer therapy by enabling targeted drug delivery, reducing harm to normal cells, and minimizing side effects, leading to better therapeutic outcomes [28,29]. A variety of therapeutic nanoparticles, such as polymeric micelles, liposomes, albumin, etc., have been successively developed with advantages of wide bioavailability, good stability, and rapid passage of biological barriers, etc., showing excellent efficacy in cancer therapy [29–32]. To address obstacles in peptide-based PROTACs, we provided a proof-of-principle design and use of nanoengineered peptide PROTACs (NP-PROTACs) for dual degradation of β-catenin and STAT3 in CRC. In this work, we first synthesized two peptide PROTACs targeting β-catenin and STAT3, respectively. Then, we designed two PEGylated peptide PROTACs via GSH-activatable disulfide bonds, which helped to self-assemble into micellar nanoparticles. The NP-PROTACs not only exhibited durable circulation stability and accumulation/responsive release in tumor sites but also potently inhibited the CRC tumor growth in mice through dual protein degradation of β-catenin and STAT3, as well as TIME remodeling, including enhanced $CD103^+$ DCs infiltration and activated T-cell cytotoxicity. This study presents a versatile nanoplatform for designing multitargeted degraders for cancer therapy, offering significant potential for clinical applications.

2. Results

2.1. β-catenin and STAT3 are co-upregulated and predict a poor prognosis in CRC

To profile β-catenin and STAT3 expression in CRC, we first analyzed data from the Cancer Proteome Atlas. The results revealed high expressions of β-catenin and STAT3 proteins in rectum adenocarcinoma (READ) and colon adenocarcinoma (COAD) tissues (Figs. S1A and B), as well as their correlation with poor prognosis (Figs. S1E and F). To further explore the correlation between β-catenin and STAT3 in CRC, we detected a significant positive correlation between β-catenin (CTNNB1) and STAT3 gene expression in tumor tissues ($P < 0.001$) based on data from the Cancer Genome Atlas (TCGA) database (Fig. 1A). Consistent with this finding, the single-cell portal data demonstrated the co-expression of the CTNNB1 and STAT3 genes in the complex cell composition of cancers (Fig. S1H). Moreover, the Wnt signaling and JAK-STAT3 pathways regulated by β-catenin and STAT3 exhibited predominantly positive correlation coefficients in the TCGA COAD cohort, indicating the frequent co-activation of these two oncogenic signals (Fig. 1B). To investigate the clinical relevance of β-catenin and STAT3 expression in CRC, we performed immunofluorescence staining assays to confirm the concurrent abundance of β-catenin and STAT3 in CRC tissues compared to paired normal tissues (Fig. 1C, Fig. S1C and D). In addition, β-catenin and STAT3 were identified as differentially expressed genes with significant upregulation in GSE31905, GSE4107, and GSE8671 datasets (Fig. 1D–G, Fig. S1G). Intriguingly, data from the single-cell portal encompassing the Human Colon Cancer Atlas (c295) supported this conclusion (Fig. 1H). Beyond co-overexpression, the levels of β-catenin and STAT3 were closely associated with a poorer prognosis in CRC patients (Fig. 1I). Categorizing CRC cases into four groups based on the expression of β-catenin and STAT3, the dual-high-expression group exhibited significantly worse disease-specific survival than both the dual-low-expression and single-high-expression groups. These data suggested that β-catenin and STAT3 were significantly increased in CRC and their co-downregulating might be a promising therapeutic strategy.

2.2. Design, synthesis, and characterization of peptide-based PROTACs

The peptide PROTAC is composed of an amino acid-encoded substrate-targeting ligand, an E3 ligase recruiting ligand, a linker, and a cell-penetrating peptide, hijacking the cellular ubiquitin-proteasome system for target protein degradation [20]. We utilized reported β-catenin- and STAT3-targeting peptide sequences as binding ligands [25,26], with von Hippel−Lindau (VHL) serving as the E3 ligand, which was linked by 6-aminohexanoic acid, forming the β-catenin-targeting PROTAC LAV and STAT3-targeting PROTAC SAV, respectively. Although their adequate affinities for the targets were confirmed by microscale thermophoresis (MST) assay (Figs. S2A and B), due to the poor membrane penetration, LAV and SAV were unable to inhibit HCT116 cell viability even at a high concentration of 40 μM (Fig. S2C). Therefore, the transmembrane peptide TAT was incorporated into the PROTAC sequence [33], resulting in the β-catenin-targeting PROTAC LAVTAT and the STAT3-targeting peptide SAVTAT (Fig. 2A and B).

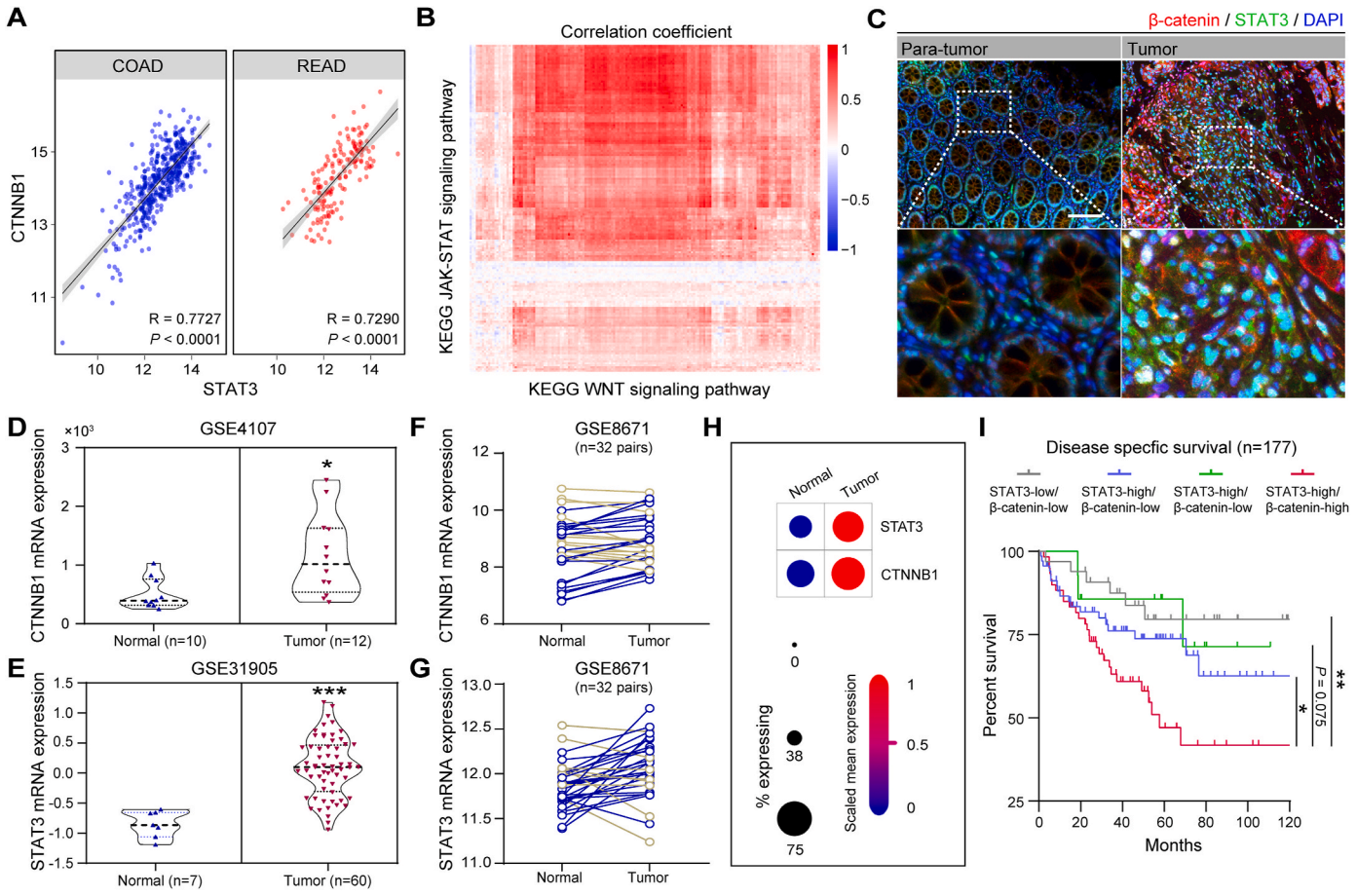

Fig. 1. β-catenin and STAT3 were two clinically significant targets in CRC. (**A**) The expressions of STAT3 and β-catenin were strongly related to CRC according to TCGA COAD and READ databases. (**B**) The correlation coefficient between the Wnt signaling pathway gene set and the JAK-STAT signaling pathway gene set in the TCGA COAD cohort (n = 453 patients). (**C**) Immunofluorescence staining assays confirmed the concurrent abundance of STAT3 and β-catenin in CRC patients compared to paired normal tissues (scale bar = 100 μm). (**D** and **F**) β-catenin and (**E** and **G**) STAT3 expression were higher than that in normal tissues according to the GSE31905, GSE4107, and GSE8617 datasets. (**H**) Single-cell RNA sequencing data from the Human Colon Cancer Atlas also suggested a higher level of STAT3 and β-catenin in tumors. (**I**) The association between the expression levels of STAT3 and β-catenin and disease-specific survival in CRC patients according to GSE17536 (n = 177 patients). *$P < 0.05$ and ***$P < 0.001$.

Next, the affinity of LAVTAT and SAVTAT for the target proteins was demonstrated through MST assay (Fig. 2C and E), with K_d values of 7.27 μM and 18.40 μM, respectively, indicating that the modification of the peptides into cell-penetrating PROTACs did not compromise their binding affinity to the targets. To assess the membrane-penetrating capability of the peptides, HCT116 cells were incubated with FITC-conjugated LAVTAT and rhodamine B-conjugated SAVTAT, respectively. Flow cytometry (Fig. S2D) and super-resolution imaging (Fig. 2D and F) demonstrated that LAVTAT and SAVTAT exhibited rapid membrane penetration kinetics, achieving saturation within 0.5–2 h. Moreover, neither LAVTAT nor SAVTAT induces hemolysis even at high concentrations of up to 80 μM, reflecting their exceptional safety profile (Fig. S2E).

Based on the above results, the antiproliferative activities of LAVTAT were demonstrated through CCK-8 assays *in vitro*, in which the IC_{50} values were 9.95 μM and 12.30 μM in HCT116 and CT26 cells, respectively (Fig. 2G). Similarly, SAVTAT inhibited the viability of CRC cells with IC_{50} values of 14.89 μM for HCT116 cells and 10.33 μM for CT26 cells (Fig. 2I). The ability of peptide PROTACs to induce target protein degradation was subsequently verified. The results revealed that LAVTAT and SAVTAT induced dose-dependent protein degradation in HCT116 (Fig. 2H and J, Fig. S2J and K) and CT26 cells (Figs. S2F–I), with a reduction of approximately 50 % at the concentration of 10 μM. Immunofluorescence staining (Fig. 2K and L) revealed a significant decrease in the levels of β-catenin and STAT3, suggesting the successful functional design of the degraders. Notably, LAVTAT did not affect other transcription complex members (GSK3β, AXIN1, or TCF4), indicating the high selectivity (Fig. 2M, Fig. S4A). The application of small molecule inhibitors targeting STAT3 is often hindered by their lack of selectivity for other members of the STAT family (STAT1, 2, 4–6). However, SAVTAT demonstrated significant selectivity for STAT3 degradation (Fig. 2N, Fig. S4B). In addition, LAVTAT and SAVTAT significantly downregulated common downstream transcriptional proteins, including the apoptosis-related proteins BCL-XL and c-Myc, as well as the cell cycle-related protein cyclin D1 (Fig. 2O, Fig. S5). Correspondingly, the flow cytometry results showed that LAVTAT and SAVTAT induced cell apoptosis and cell cycle arrest in HCT116 cells (Fig. S6).

To further validate the impact of β-catenin and STAT3 degradation on downstream cellular signaling pathways, HCT116 cells were treated with LAVTAT or SAVTAT for 12 h, followed by RNA extraction for transcriptomic analysis. The results revealed that LAVTAT induced significant downregulation of Wnt signaling pathways, especially ubiquitin-mediated proteolysis and the cell cycle-related pathway ($P = 0.0012$) (Figs. S7A and C). SAVTAT induced a noticeable increase in the levels of multiple immune-related downstream signaling pathways (Figs. S7B and D). From a transcriptomic perspective, these findings confirmed that both LAVTAT and SAVTAT could modulate downstream signals associated with β-catenin and STAT3. To explore the potential synergistic impact of co-degrading STAT3 and β-catenin, as well as to

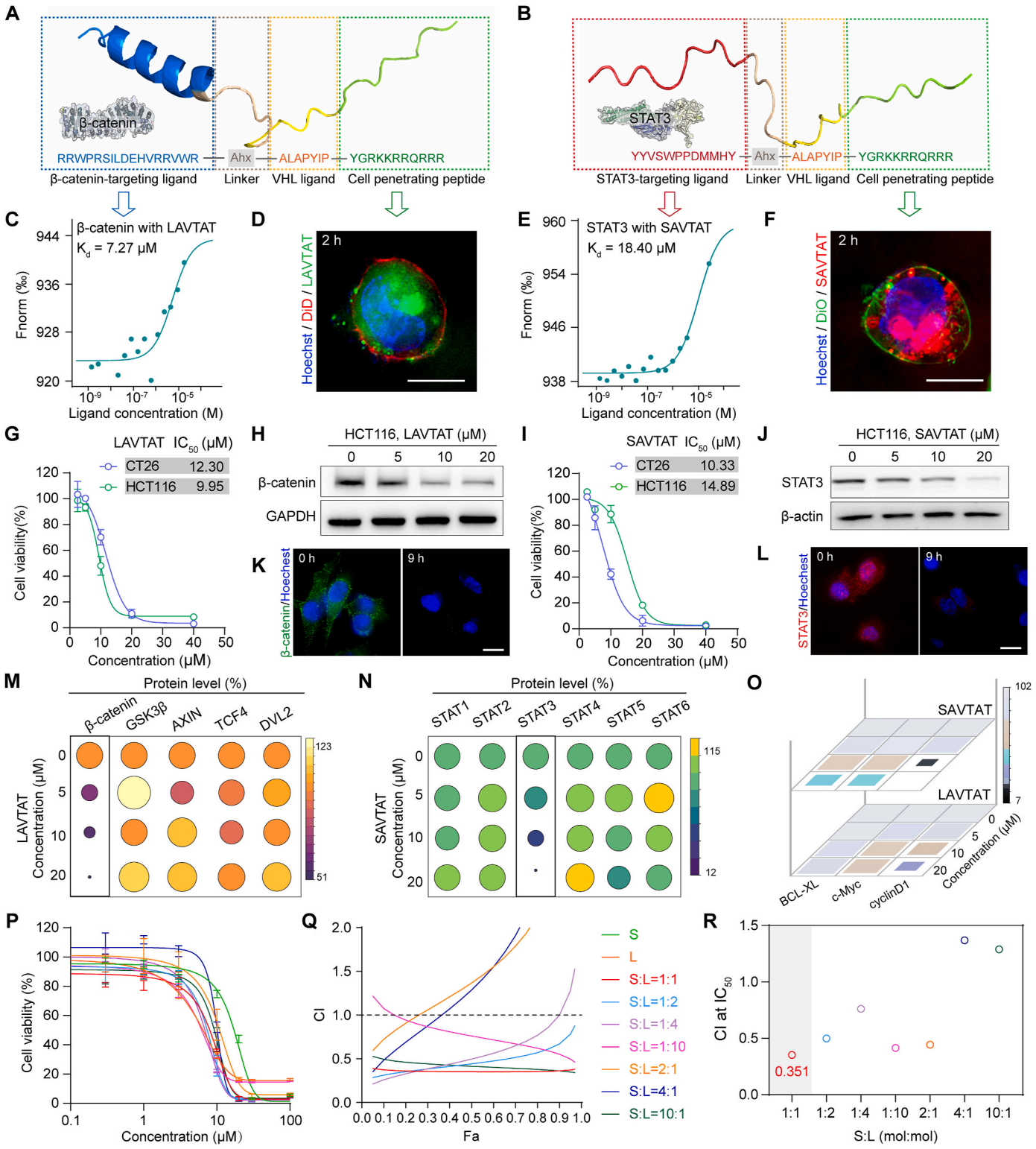

Fig. 2. Design, synthesis, and characterization of LAVTAT and SAVTAT. Schematic illustration and sequences of LAVTAT (**A**) and SAVTAT (**B**). (**C**) MST analysis of LAVTAT binding to β-catenin (K_d = 7.27 μM). (**D**) Super-resolution imaging showing that LAVTAT with a FITC label penetrated the cell membrane at 2 h (scale bar = 10 μm). (**E**) MST analysis of SAVTAT binding to STAT3 (K_d = 18.4 μM). (**F**) Super-resolution imaging showed that SAVTAT with the RhodB label penetrated the cell membrane at 2 h (scale bar = 10 μm). (**G**) CCK8 assays showed that LAVTAT inhibited the viability of CT26 (IC_{50} = 12.3 μM) and HCT116 cells (IC_{50} = 9.95 μM) in a dose-dependent manner. (**H** and **K**) The ability of LAVTAT to degrade β-catenin in HCT116 cells after treatment for 12 h was verified through Western blot analysis and immunofluorescence (scale bar = 15 μm). (**I**) CCK8 assays showed that SAVTAT caused dose-dependent inhibition in CT26 (IC_{50} = 10.33 μM) and HCT116 cells (IC_{50} = 14.89 μM). (**J** and **L**) The ability of SAVTAT to degrade STAT3 in HCT116 cells after treatment for 12 h was verified through Western blot analysis and immunofluorescence (scale bar = 15 μm). (**M**) LAVTAT had significant selectivity for β-catenin degradation over other members of the β-catenin transcriptional complex, and (**N**) SAVTAT had significant selectivity for STAT3 degradation over other members of the STAT family. (**O**) Western blot analysis of the effects on downstream proteins induced by SAVTAT and LAVTAT. (**P**–**R**) HCT116 cells were treated with different concentrations of LAVTAT and SAVTAT, and the CI values were calculated according to the CCK8 assay results. Data were presented as mean ± SD; n = 3.

determine the optimal concentration ratio for achieving the maximum synergistic effect between the two degraders, HCT116 cells were treated with various ratios of LAVTAT and SAVTAT, and cell viability was determined by a CCK8 assay (Fig. 2P). The results revealed that co-administration of LAVTAT and SAVTAT at multiple concentration ratios had synergistic cytotoxicity against HCT116 cells (Fig. 2Q), and the maximum synergistic effect was observed at a concentration ratio of 1: 1 with a cooperative index (CI) of 0.351 (Fig. 2R).

2.3. PROTACs degrade target proteins through the ubiquitin-proteasome system

The protein degradation mechanisms of LAVTAT and SAVTAT were subsequently studied. As reported, PROTACs bind to target proteins and recruit the E3 ubiquitin ligase VHL, forming a ternary complex. Subsequently, VHL ubiquitinates the target protein, and ubiquitin tags are recognized by the proteasome, leading to protein degradation [22]. After HCT116 cells were treated with 10 μM LAVTAT or SAVTAT for 12 h, a significant increase in protein ubiquitination expression was observed, suggesting that target proteins were ubiquitinated during peptide PROTAC-induced degradation (Fig. 3A). Preincubation of HCT116 cells with 15 mM VHL ligand for 4 h followed by the addition of 10 μM PROTACs for 12 h, competitively blocked the protein degradation, confirming the dependence of the degradation process on VHL recruitment (Fig. 3B and C). Furthermore, co-treatment with the proteasome inhibitor MG-132 (5 μM) and PROTAC (20 μM) for 12 h resulted

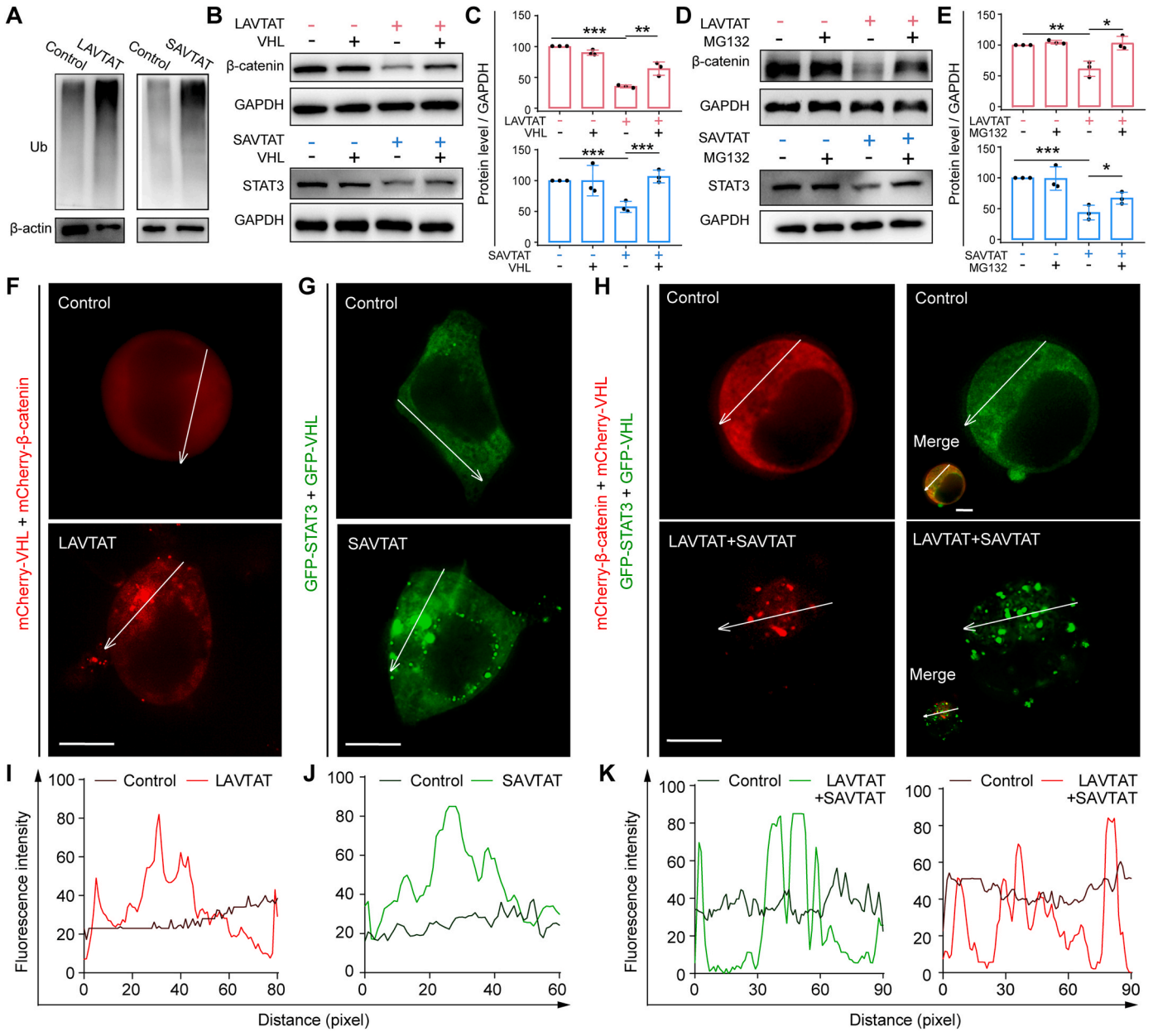

Fig. 3. Mechanistic studies of LAVTAT- and SAVTAT-induced targeted protein degradation. (**A**) Western blot detection of ubiquitin proteins revealed that LAVTAT and SAVTAT caused an increase in the ubiquitin signal after LAVTAT or SAVTAT treatment for 12 h in HCT116 cells. (**B** and **C**) Western blot analysis suggested that excessive VHL levels blocked the degradation of LAVTAT and SAVTAT. (**D** and **E**) Western blot results suggested MG132 blocked the degradation of LAVTAT and SAVTAT. Transient transfection studies were conducted in HEK 293T cells, and images were acquired after 2 h of LAVTAT and/or SAVTAT treatment. Bright fluorescent droplets represented the formation of the target-PROTAC-VHL ternary complex. (**F** and **I**) LAVTAT caused β-catenin-LAVTAT-VHL ternary complex formation (scale bars = 10 μm). (**G** and **J**) SAVTAT caused STAT3-SAVTAT-VHL ternary complex formation (scale bars = 10 μm). (**H** and **K**) LAVTAT and SAVTAT caused ternary complex formation simultaneously (scale bars = 10 μm). Data were presented as mean ± SD; n = 3. *$P < 0.05$, **$P < 0.01$, and ***$P < 0.001$.

in the preservation of the target proteins, confirming the dependence of the degradation process on the proteasome (Fig. 3D and E). To detect the formation of the ternary complex induced by LAVTAT, β-catenin, and VHL plasmids were labeled with enhanced mCherry and a homologous oligomerization tag (HOTag), respectively, forming the β-catenin-mCherry-HOTag6 and VHL-mCherry-HOTag3, which were then transfected into cells. Similarly, STAT3-EGFP-HOTag6 and VHL-EGFP-HOTag3 were co-transfected into cells to detect the formation of a ternary complex induced by SAVTAT. According to the principle of the SPPIER assay, once PROTACs bring together the target

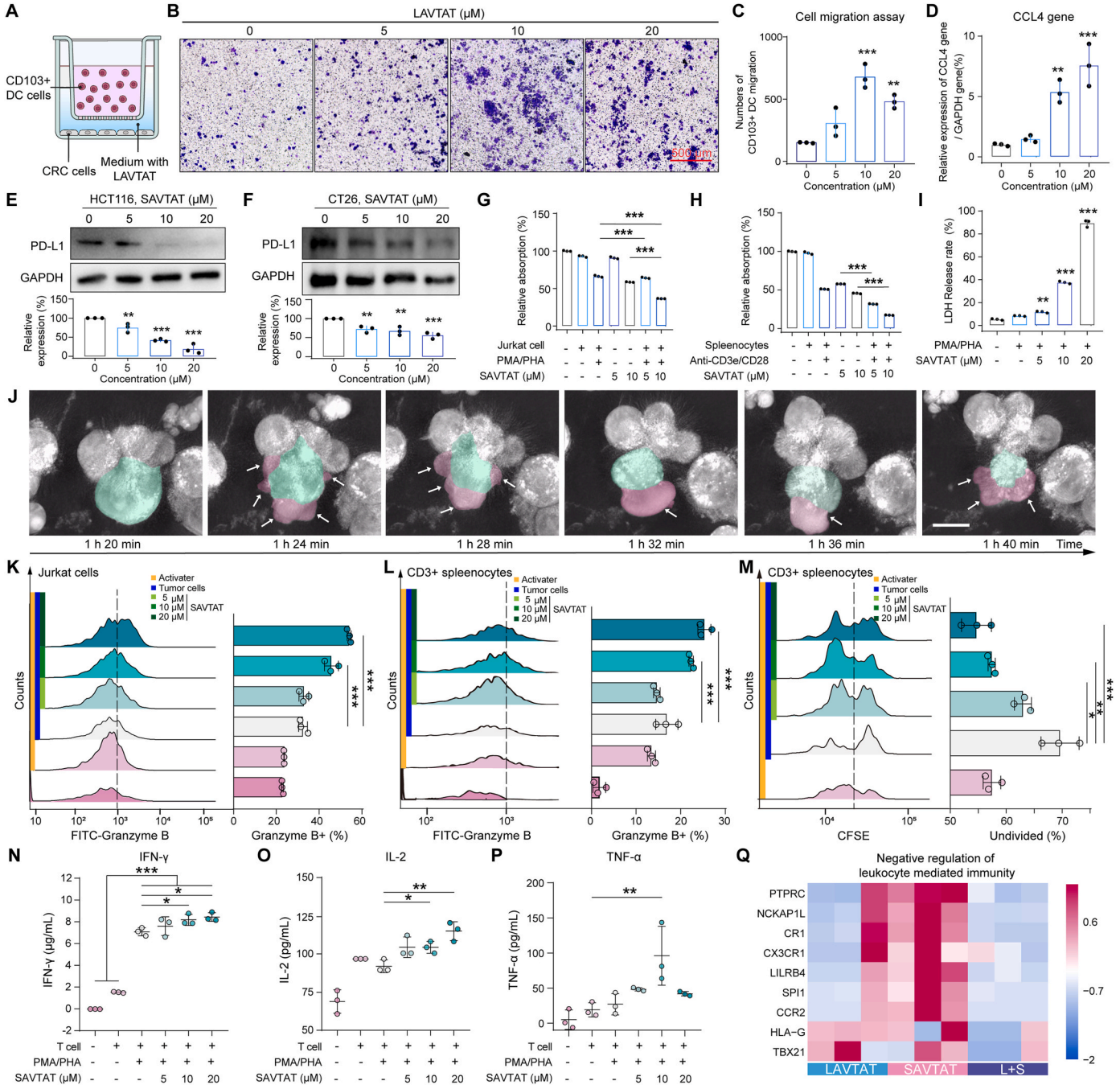

Fig. 4. LAVTAT and SAVTAT improved the tumor immunosuppressive microenvironment *in vitro*. **(A)** Schematic diagram of increased CD103$^+$ DC migration induced by LAVTAT. **(B** and **C)** LAVTAT promoted CD103$^+$ DC migration to CT26 cells (scale bar = 500 μm). **(D)** qRT-PCR results revealed that LAVTAT increased CCL4 gene expression in CT26 cells. **(E** and **F)** SAVTAT downregulated PD-L1 protein expression in HCT116 and CT26 cells. **(G)** HCT116 cells were co-cultured with inactivated or activated Jurkat cells (HCT116: Jurkat = 1:6) for 48 h after pretreatment with SAVTAT. Cell survival was analyzed using a crystal violet staining assay. **(H)** CT26 cells were co-cultured with inactivated or activated mouse spleen-derived T cells (CT26: Jurkat = 1:10) for 24 h after pretreatment with various concentrations of SAVTAT. The cell survival rates were analyzed using a crystal violet staining assay. **(I)** LDH assays revealed that SAVTAT treatment and subsequent T-cell culture caused lysis of CT26 cells. **(J)** Live cell imaging videos showing the interaction between Jurkat and SAVTAT-treated HCT116 cells and that Jurkat cells-induced HCT116 cells lysis at approximately 1.5 h (scale bar = 10 μm). **(K** and **L)** Flow cytometry exhibited that SAVTAT increased Granzyme B secretion. **(M)** Flow cytometry revealed that SAVTAT increased T cell proliferation. **(N, O,** and **P)** ELISA results showed that SAVTAT increased IFN-γ, IL-2, and TNF-α levels. Transcriptomic analysis of HCT116 cells showed that co-administration of LAVTAT and SAVTAT significantly decreased the expression of immune suppression genes. The data were presented as the mean ± SD; n = 3. *$P < 0.05$, **$P < 0.01$, and ***$P < 0.001$.

protein and VHL, the fluorescent aggregates form bright droplets [34], with red and green representing the formation of the ternary complexes induced by β-catenin and STAT3, respectively. LAVTAT induced the formation of red fluorescent droplets (Fig. 3F and I), while SAVTAT induced the formation of green fluorescent droplets (Fig. 3G and J). The simultaneous addition of these two PROTACs resulted in the emergence of both types of droplets, confirming that both PROTACs could mediate the formation of the ternary complexes within cells (Fig. 3H and K).

2.4. PROTACs enhance the recruitment of CD103$^+$ DCs and stimulated T cell activity

As previously mentioned, β-catenin decreased the infiltration of CD103$^+$ DCs into the melanoma microenvironment by inhibiting the expression of CCL4, consequently reducing the infiltration of CD8$^+$ T cells [16]. After investigating transcriptomic data from 453 CRC patients in the GDC database and calculating the correlation between the proportions of tumor-infiltrating CD8$^+$ T cells and β-catenin expression using the Cibersort algorithm, a significant negative correlation was detected (Fig. S8A). To investigate whether degrading β-catenin could increase the recruitment of CD103$^+$ DCs, mouse bone marrow-derived monocytes were induced to differentiate into CD103$^+$ DCs by stimulation with 10 ng/mL GM-CSF and 200 ng/mL FLT3L for 10 days. The flow cytometry results confirmed the successful induction of CD103$^+$ DCs, with a percentage of 92.95 % (Fig. S8B). Then, the induced CD103$^+$ DCs were placed in the upper chamber for membrane fusion 1.5 h in advance (Fig. 4A). The lower chamber liquid was then replaced with supernatant from CT26 cells treated with different concentrations of LAVTAT. After 4 h, there was a significant increase in the migration of CD103$^+$ DCs in the LAVTAT group (Fig. 4B and C). In the 10 μM group, migration increased 4.51 times compared to the control group. In the 20 μM group, migration was slightly weaker than that in the 10 μM group, possibly due to the high dose of LAVTAT causing toxicity to CT26 cells, leading to cell death and their limited secretion of CCL4. The expression level of CCL4 mRNA in CT26 cells after LAVTAT treatment increased in a dose-dependent manner, confirming the mechanism of increased recruitment of CD103$^+$ DCs (Fig. 4D).

Given that the JAK-STAT3 pathway is closely related to tumor immunity, the impact of STAT3 degradation on T-cell activity was then detected after HCT116 or CT26 cells were incubated with SAVTAT. After treatment with SAVTAT, co-culture experiments were conducted with the corresponding human T cells (Jurkat cells) or mouse spleen lymphocytes. On the one hand, dose-dependent downregulation of PD-L1 was observed in both HCT116 and CT26 cells after treatment with SAVTAT (Fig. 4E and F). On the other hand, synergistic killing of tumor cells by STAT3 degradation and the presence of cytotoxic T cells was revealed (Fig. 4G, H and I, Fig. S9). These findings suggested the potential enhancement of T-cell function in co-culture experiments. NanoLive 3D Explorer was further used to observe the Jurkat cells-mediated killing effect after SAVTAT treatment for 4 h (Fig. 4J, Movie S1). We observed that Jurkat cells caused the bubbling and contraction of HCT116 cells. Additionally, T cells in the treated group exhibited significantly greater secretion of Granzyme B (Fig. 4K and L), IFN-γ (Fig. 4N), IL-2 (Fig. 4O), and TNF-α (Fig. 4P), which are known as cytotoxic T cells. CFSE flow cytometry revealed that the presence of tumor cells inhibited T-cell proliferation, while T cells in the SAVTAT-treated group returned to the level observed in the co-culture without tumor cells and even exhibited a greater proliferation rate (Fig. 4M). Transcriptomic data revealed that when HCT116 cells were treated with the same total concentration of LAVTAT and/or SAVTAT, the combined treatment group exhibited the most significant downregulation of tumor immune suppression-related genes. These findings indicated that the combination therapy with these two PROTACs synergistically inhibited CRC cell viability and synergistically improved the TIME (Fig. 4Q).

2.5. Preparation and characterization of NP-PROTACs

To fabricate NP-PROTACs, we first connected LAVTAT and SAVTAT separately to DSPE-PEG$_{2000}$-SH via disulfide bonds to form DSPE-PEG$_{2000}$-PROTACs. Since the maximum synergistic effect was achieved when the molar ratio of LAVTAT to SAVTAT was 1:1 (Fig. 2R), the NP-PROTACs were formed by the thin-film dispersion method when the ratio of two PEGylated PROTACs was 1:1 (Fig. 5A). The core of NP-PROTAC consisted of hydrophobic lipids, the middle layer contained PEG$_{2000}$, and the PEG segments were linked to the outermost layer of the micelle through disulfide bonds with the respective peptide PROTACs.

Dynamic light scattering revealed that the NP-PROTACs had an average hydrodynamic diameter of 130 nm (Fig. 5B) and a zeta potential of 17.8 mV (Fig. 5C). The morphology was determined by transmission electron microscopy (TEM), which showed that the NP-PROTACs were nanometer-sized spherical particles (Fig. 5B). To confirm the co-loading of both peptide PROTACs into NP-PROTACs, FITC-LAVTAT and rhodamine B-SAVTAT were used to prepare fluorescently labeled micelles. Subsequently, we assessed the fluorescence intensity in HCT116 cells after incubation with fluorescent micelles using flow cytometry. Both fluorescent signals were synchronously taken up by the cells, reaching saturation at approximately 2 h (Fig. 5D and E). The intensities of the two fluorescence signals were strongly positively correlated, with almost no cells showing single-fluorescence positivity. Super-resolution imaging also demonstrated the co-localization and enrichment of both fluorescence signals within HCT116 cells (Fig. 5F). The peak heights overlapped, indicating the successful co-loading of both LAVTAT and SAVTAT within the NP-PROTACs (Fig. 5G).

To verify the reducibility of NP-PROTACs, the micelles were incubated in PBS containing 10 μM DTT for 3 h at 37 °C. Under PBS conditions, the size of the NP-PROTACs remained uniform, while a significant particle size split occurred under DTT conditions, confirming the ability of the NP-PROTACs to be cleaved (Fig. 5H). Subsequently, a dialysis method was employed to investigate the release profiles of the NP-PROTACs. The release ratio of both LAVTAT and SAVTAT approached 80 % at 9 h after DTT treatment, while the release of LAVTAT and SAVTAT was significantly slower under PBS conditions, reaching approximately 40 % at 24 h (Fig. 5I). These results verified the reducibility of NP-PROTACs *in vitro*. When we detected the anti-proliferative activities of NP-PROTACs, IC_{50} values of 9.43 μM and 6.67 μM were obtained for HCT116 and CT26 cells, respectively (Fig. 5J). Of note, NP-PROTACs did not significantly affect the viability of normal colonic epithelial cells (NCM460) (Fig. 5J), which may be attributed to the relatively lower GSH concentration in normal cells than in tumor cells. NP-PROTACs also did not induce hemolysis at high concentrations of up to 40 μM, reflecting an exceptional safety profile (Fig. S12A). Moreover, NP-PROTACs degraded both STAT3 and β-catenin after 24 h of incubation in HCT116 cells (Fig. 5K and L).

2.6. Biodistribution of NP-PROTACs

To assess the biodistribution of the NP-PROTACs, SAVTAT was labeled with Cy5.5, and LAVTAT was labeled with ICG. When the tumor volume reached about 200 mm^3, CT26-bearing BALB/c mice were injected via the tail vein with 100 μL of free fluorescently labeled LAVTAT and SAVTAT or fluorescently labeled NP-PROTACs (0.25 mg/kg ICG and 0.25 mg/kg Cy5.5). At 1, 3, 6, 9, 12, and 24 h after injection, *in vivo* near-infrared fluorescence imaging was used to detect the distribution of ICG and Cy5.5 (Fig. 6A). The fluorescent signal of NP-PROTACs was distinct in the tumor area after 1 h, and there was still a strong signal at 24 h, suggesting that NP-PROTACs could be retained in the tumor areas for a longer time than free PROTACs (Fig. 6A and B). 24 h after injection, the tumors were collected and studied. According to tumor images (Fig. 6C) and cryosectioned tumor tissue results (Fig. 6D), the fluorescence signals of ICG and Cy5.5 strongly colocalized, indicating the co-localization of LAVTAT and SAVTAT *in vivo*. Notably, the

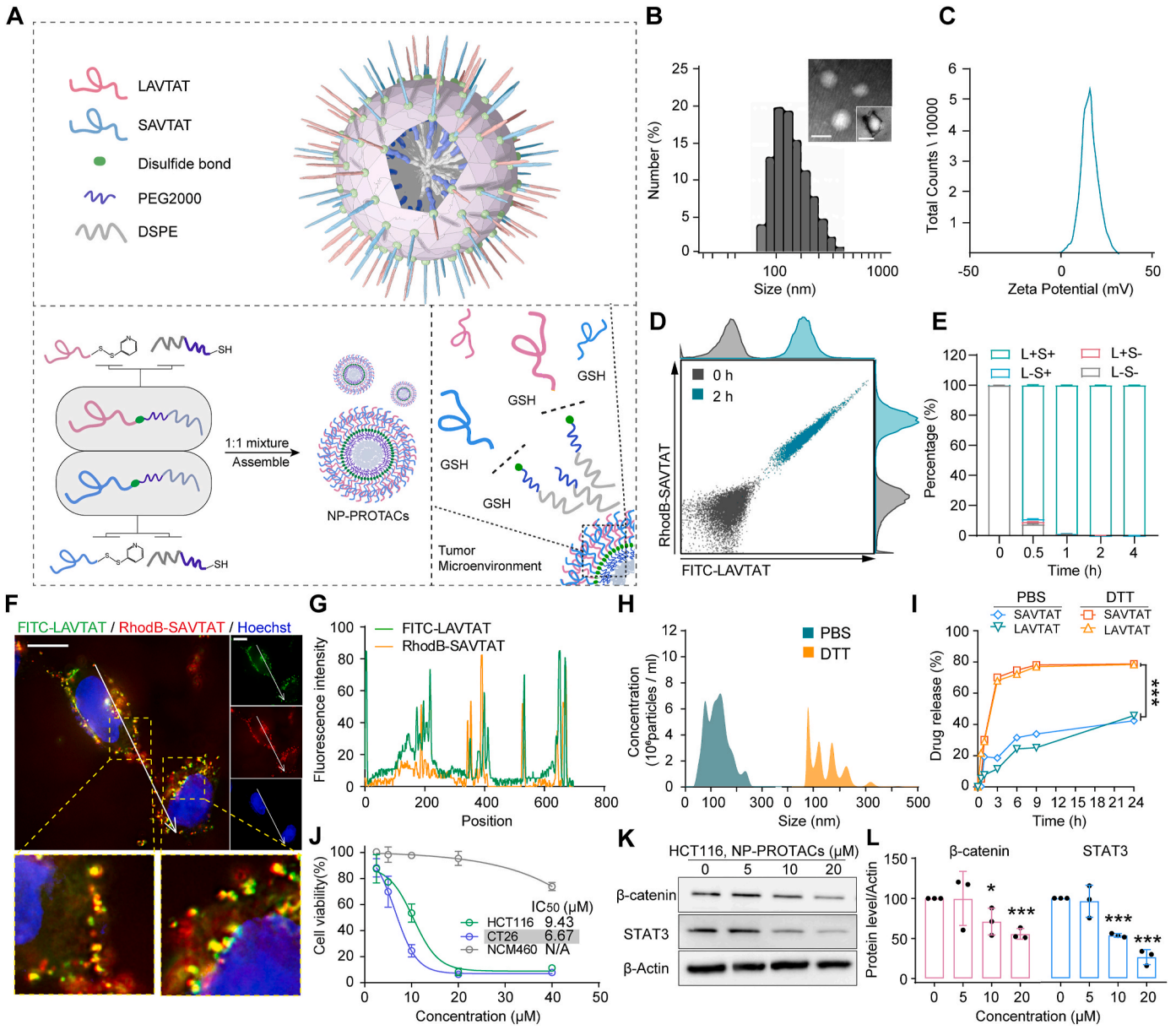

Fig. 5. Design, synthesis, and characterization of NP-PROTACs. (**A**) Schematic diagram and synthesis of NP-PROTACs. (**B**) Size and TEM images of NP-PROTACs (scale bars = 200 μm). (**C**) Zeta potential of NP-PROTACs. (**D**) Flow cytometry showed that fluorescently labeled NP-PROTACs penetrated the cell membrane after 2 h, and carried equivalent amounts of LAVTAT and SAVTAT into the HCT116 cells. (**E**) Statistical analysis of fluorescent signals at 0, 0.5, 1, 2, and 4 h. (**F** and **G**) After treatment with fluorescently labeled NP-PROTACs for 2 h, LAVTAT and SAVTAT signals strongly colocalized in HCT116 cells (scale bar = 15 μm). (**H**) Nanoparticle tracking analysis showed that NP-PROTACs were reduction-responsive in size distribution. (**I**) Drug release assay showed that the release of NP-PROTACs occurred in a reduction-responsive manner. (**J**) CCK-8 assay of NP-PROTACs in CT26, HCT116, and NCM460 cells. (**K** and **L**) Western blot results showed that NP-PROTACs caused the degradation of STAT3 and β-catenin in HCT116 cells. The data were presented as the mean ± SD; n = 3. $^{*}P < 0.05$, $^{**}P < 0.01$, and $^{***}P < 0.001$.

peak time and clearance rate of SAVTAT in tumor tissue were slightly lower than those of LAVTAT. However, for NP-PROTACs, the peak time and clearance rate of both fluorescent signals were consistent, indicating a stable ratio of LAVTAT to SAVTAT, which helped to maximize the synergistic effect. These data confirmed that NP-PROTACs could be enriched at the tumor site and exhibited longer retention than free PROTACs after systemic injection, providing an excellent reference for applying peptide PROTACs *in vivo*.

To evaluate the targeting efficiency and safety of NP-PROTACs, we conducted a biodistribution experiment in mice using NP-PROTACs loading DiR (named DiR@NP-PROTACs) and free DiR. *In vivo* imaging exhibited that although DiR@NP-PROTACs and free DiR were enriched in the liver, NP-PROTACs significantly enhanced the tumor-targeting ability of DiR (Figs. S12B–D). Moreover, protein expression of STAT3 or β-catenin in liver and lung tissues was not affected after NP-PROTACs treatment, indicating the safety of NP-PROTACs (Fig. S12E).

2.7. Antitumor efficacy of NP-PROTAC in vivo

To evaluate the antitumor effects of NP-PROTACs in a xenograft tumor model derived from CT26 cells, the mice were intravenously injected with NP-PROTACs (containing 2.5 mg/kg LAVTAT and 2.5 mg/kg SAVTAT) or single-agent micelles containing LAVTAT or SAVTAT (5 mg/kg each, abbreviated as NP-L or NP-S). The treatment schedule is shown in Fig. 7A. Compared to those in the control group, NP-PROTACs, NP-Ls, and NP-Ss induced significant tumor regression (Fig. 7B and C)

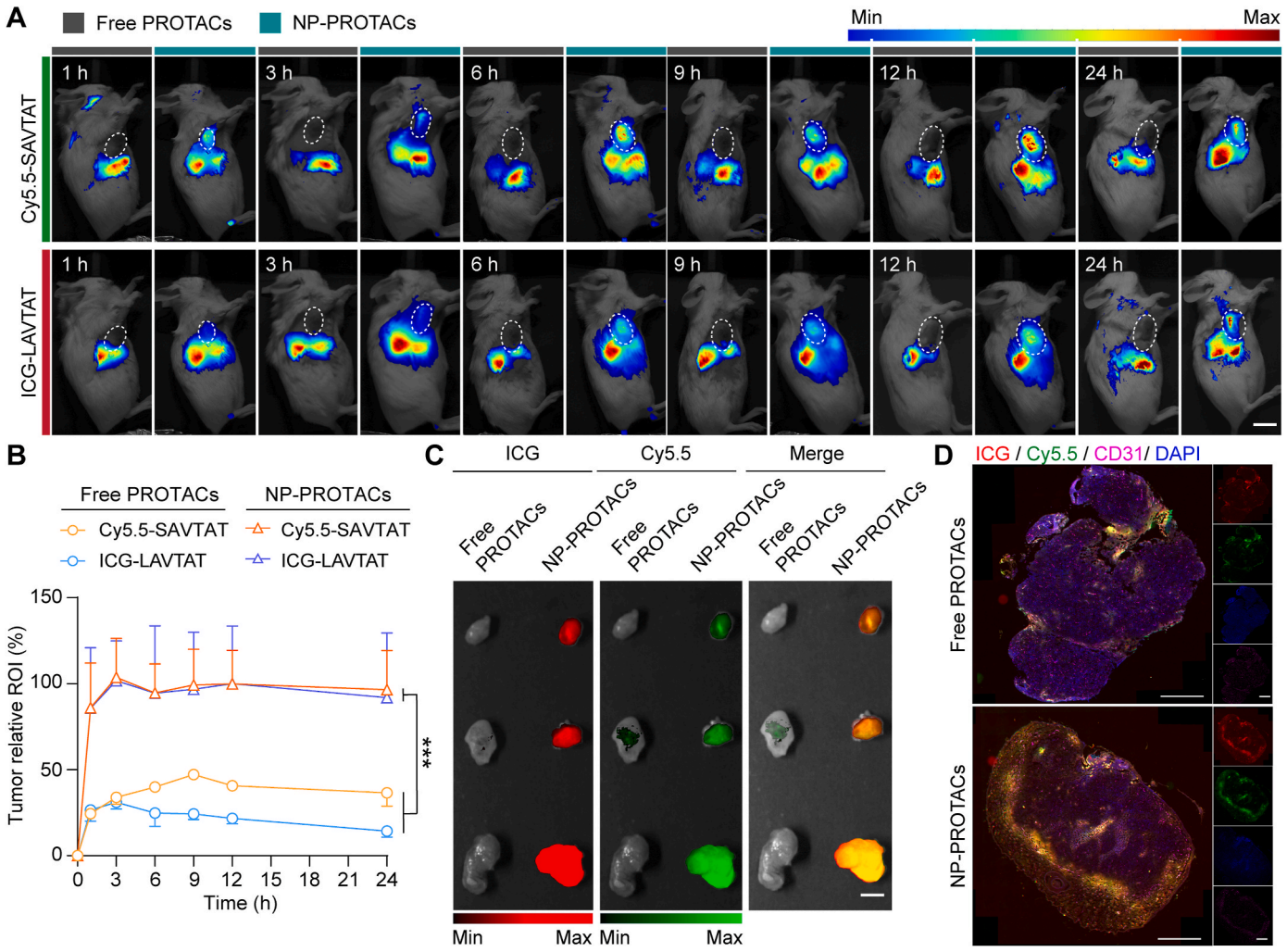

Fig. 6. *In vivo* tumor targeting ability of NP-PROTACs. (**A**) Female BALB/c mice bearing CT26 tumors (~200 mm^3) were given a single intravenous injection of a mixture of ICG-labeled LAVTAT and Cy5.5-labeled SAVTAT or NP-PROTACs. At 1, 3, 6, 9, 12, and 24 h after injection, mice with *in vivo* fluorescence were imaged by a Bio Imaging Technology system (scale bar = 1 cm). (**B**) After injection, the average radiant efficiency of tumors *in vivo* at 1, 3, 6, 9, 12, and 24 h. (**C**) At 24 h after injection, the mice were sacrificed, and the tumors were harvested for ex vivo imaging (scale bar = 0.5 cm). (**D**) Distribution of ICG-labeled LAVTAT, Cy5.5-labeled SAVTAT, and NP-PROTACs in cryosectioned tumor tissues. The data were presented as the mean ± SD; n = 3. ***$P < 0.001$.

and reduced tumor weight (Fig. 7D) without affecting body weight (Fig. 7E). Furthermore, the results of routine blood tests revealed the excellent safety of the micelles *in vivo* (Fig. S13).

Notably, the antitumor effect of NP-PROTACs was significantly more significant than that of NP-L or NP-S. Subsequent H&E staining, TUNEL assays, and Ki67 analysis (Figs. S14A–D) of tumor slices indicated that NP-PROTACs treatment led to more significant apoptosis and necrosis and decreased proliferating cell numbers than single-target treatments. H&E staining of major organs (heart, liver, spleen, lung, and kidney) also proved the good safety of NP-PROTACs (Fig. S14E). Western blotting and immunofluorescence staining results showed that NP-PROTACs and single-target micelles mediated the degradation of their respective targeted proteins (STAT3 and/or β-catenin) (Fig. 7F–J). Despite lower levels of STAT3 in two tumor tissues from the NP-S group compared to those in the NP-PROTACs group due to higher SAVTAT doses in the former (Fig. 7G), treatment with NP-PROTACs exhibited synergistic therapeutic benefits of simultaneous degradation of both STAT3 and β-catenin. In summary, NP-PROTACs inhibited tumor growth by reducing STAT3 and β-catenin protein levels, inducing tumor apoptosis and necrosis, and suppressing tumor proliferation.

To investigate the impact of NP-PROTACs on the TIME, a flow cytometry assay was used to detect the infiltration and activation of $CD8^+$ T cells, $CD4^+$ T cells, $CD103^+$ DCs, and macrophages in tumor tissues (Fig. 7K–O, Fig. S15). The results indicated a significant increase in the infiltration of $CD103^+$ DCs when β-catenin was degraded (Fig. 7K and O, Fig. S16) and an increase in Th1 cell infiltration when STAT3 was degraded (Fig. 7O, Fig. S15B, and Fig. S20). The infiltration of $CD8^+$ cells increased to varying degrees in all three treatment groups (Fig. 7O, Fig. S15A, and Fig. S17). Significantly, compared to those in the single-target degradation group, the levels of the cytotoxicity-related markers Granzyme B (Fig. 7L and O, Fig. S19) and IFN-γ (Fig. 7M and O, Fig. S18), which represent the activation of $CD8^+$ T cells, were significantly elevated after NP-PROTACs treatment, indicating increased activation of T-cell functions in the TIME.

Regulating tumor-associated macrophages can inhibit tumor growth by mediating immune microenvironment [35]. Simultaneous degradation of both STAT3 and β-catenin significantly reduced the numbers of M2-type macrophages that promoted tumor progression (Fig. 7N and O, Fig. S21C) while enhancing the numbers of M1-type macrophages to varying degrees in all three treatment groups (Fig. 7O, Fig. S15C, Fig. S21B). These results suggest that NP-PROTACs enhanced the functions of various immune cells in the TIME, simultaneously boosting adaptive immunity (including T cells and DCs) and innate immunity (macrophages).

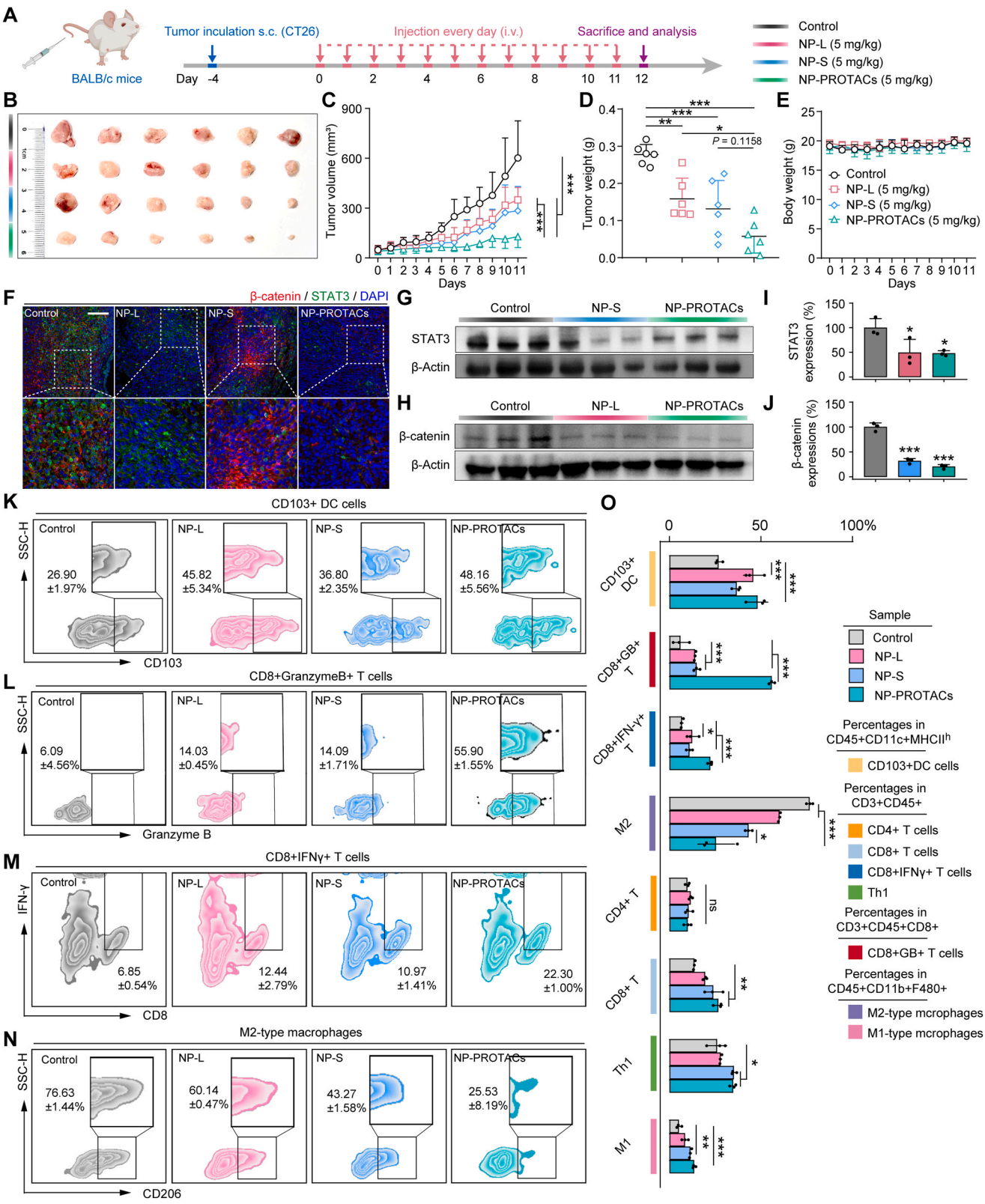

Fig. 7. NP-PROTACs degraded STAT3 and β-catenin, improving the TIME *in vivo*. (**A**) Treatment regimen diagrams (n = 6). (**B** and **D**) After the mice were sacrificed, the tumors were photographed, and the tumor weights were recorded. (**C** and **E**) Both tumor volume and body weight were monitored every day. (**F**) Immunofluorescence staining of tumor tissue revealed the downregulated target protein in each treatment group (scale bars = 100 μm). (**G**–**J**) Western blot analyses showed that micelle treatment inhibited β-catenin and/or STAT3 levels *in vivo*. (**K**–**N**) The levels of CD103 in DCs, the levels of granzyme B and IFN-γ in T cells, and the polarization of M2-type macrophages were analyzed through flow cytometry (n = 3). (**O**) The statistics of the above immune cells were presented as bars, and $CD4^+$T cell, $CD8^+$T cell, Th1 infiltration, and polarization of M2-type macrophages were also determined by flow cytometry and were presented. The data were presented as the mean ± SD. *$P < 0.05$, **$P < 0.01$, and ***$P < 0.001$.

2.8. NP-PROTACs demonstrate excellent efficacy in CRC PDO and PDX models

Patient-derived organoids (PDOs) have become an effective clinically relevant model for predicting drug responses [36] because they retain the morphology and characteristics of human primary tumors (Fig. 8A). To assess the potential clinical application of NP-PROTACs further, we used PDOs derived from three CRC patients as models. PDOs were treated with different concentrations of NP-PROTACs. Images were collected before treatment (day 0) and on day 6, and the inhibition of organoid growth by the drug was calculated based on the maximum cross-sectional area. Subsequently, bright-field images were captured, and the LIVE/DEAD staining method was used to label live organoids as green and dead organoids as red (Fig. 8E). These results demonstrated that NP-PROTACs significantly reduced the number and viability of CRC organoids, with IC_{50} values ranging from 3.29 to 8.97 μM (Fig. 8B–D).

Patient-derived xenografts (PDX) models that recapitulate the biological properties and molecular heterogeneity of human cancers have been considered an ideal preclinical model [37]. We further validated the efficacy of NP-PROTACs in CRC PDX models. As the PDX volume reached approximately 100 mm^3, these mice were randomly divided into 2 groups and intravenously administrated with PBS or NP-PROTACs (10 mg/kg/day). NP-PROTACs effectively inhibited the PDX tumor progression with good safety (Fig. 8F–H), highlighting its efficacy in clinically relevant tumor models.

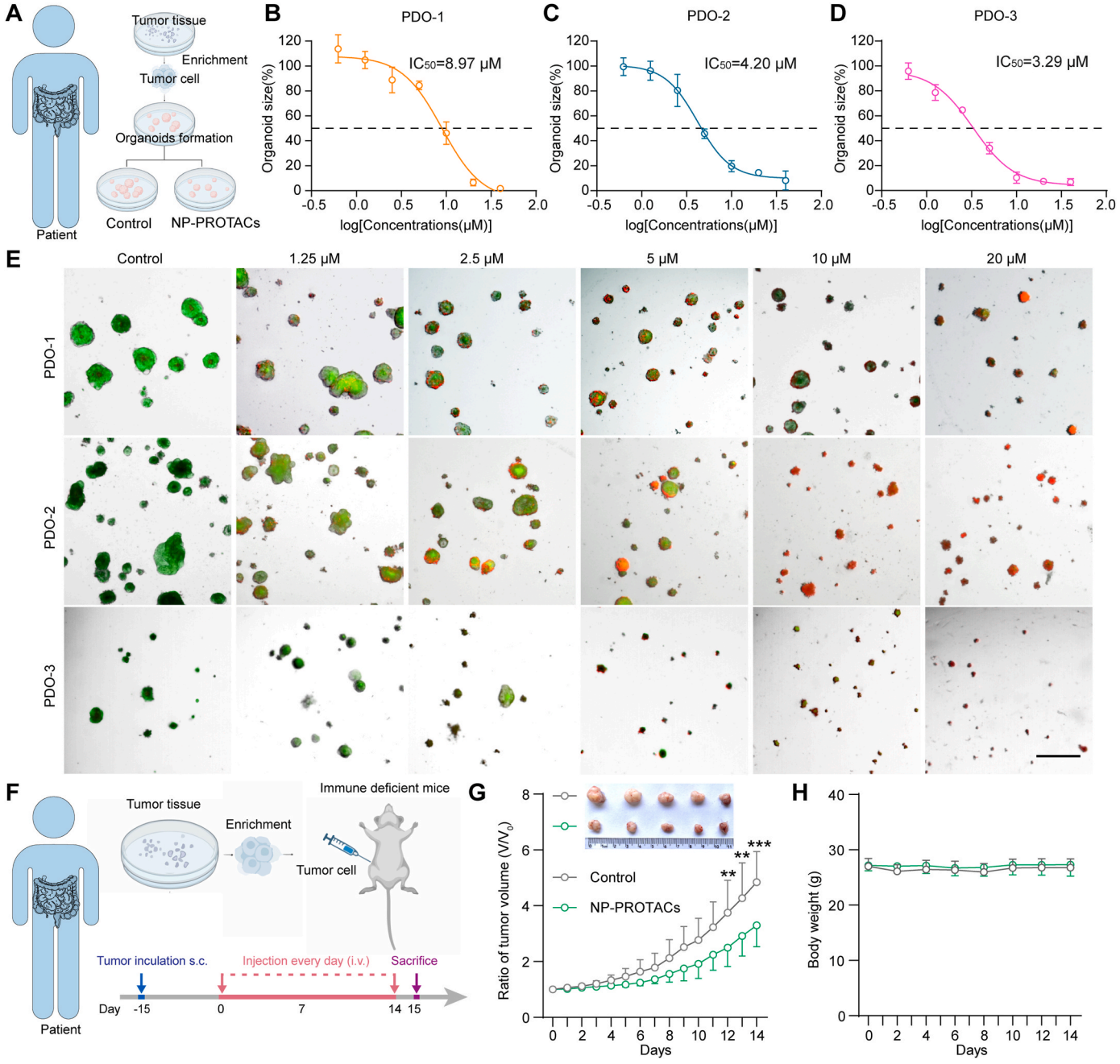

Fig. 8. NP-PROTACs inhibited the growth of CRC tumors in organoid and PDX models. **(A)** The pattern diagram of organoids. **(B–D)** Inhibitory effects of NP-PROTACs on organoids based on organoid size (%) (n = 3 replicates). **(E)** Images of PDOs stained with Live/Dead fluorescent dye (scale bars = 200 μm) after NP-PROTACs treatment for 6 days (n = 3 replicates). **(F)** The pattern diagram of the PDX model. **(G)** Relative volume curves of tumor growth and tumor photos in different groups (n = 5). **(H)** Body weight of mice (n = 5). $^{**}P < 0.01$, and $^{***}P < 0.001$.

3. Discussion

Currently, combination therapy targeting multiple pathways has emerged as a prominent development trend in cancer therapy owing to its remarkable efficacy and reduced likelihood of resistance [38]. Moreover, emerging research has focused on dual-target degradation rather than dual-target inhibition [39,40]. This study (Fig. 9) focused on the commonly activated Wnt/β-catenin and JAK/STAT pathways in CRC. Our analysis revealed frequent co-overexpression of the critical effectors β-catenin and STAT3 in tumor tissues, which are closely associated with cancer prognosis. We further found that the simultaneous degradation of β-catenin and STAT3 at both cellular and *in vivo* levels synergistically impedes tumor growth, highlighting the potential therapeutic benefits and immune-activating capabilities of dual-target degradation compared to single-target degradation in CRC treatment. Significantly, the administration of NP-PROTACs at a comparatively lower dosage exhibited enhanced efficacy, indicating favorable safety profiles for dual-target degradation in clinical use. This endeavor may not only uncover the potential of existing drugs but also provide valuable insights into targeted therapy against candidate targets.

Immunotherapy has emerged as a prominent area of research in CRC treatment in recent years. Notably, patients with mismatch repair gene defects (dMMR) or microsatellite highly unstable (MSI-H) phenotypes have shown remarkable benefits from immune checkpoint inhibitors with pathological complete response rates ranging from 60 % to 67 % [41]. However, the majority of patients with proficient mismatch repair (pMMR) or microsatellite stable (MSS) CRC demonstrate a limited response to immune checkpoint inhibitors [42]. The interaction between cancer cells and the immune system is a systematic multi-step process. Improving a single mechanism offers limited efficacy for immunologically "cold" tumors, providing us with insights. Hence, applying immune combination therapy to elicit a tumor-specific immune response via chemotherapy or targeted therapy represents a pivotal avenue of investigation in this field. This study confirmed that the dual degradation of β-catenin and STAT3 can effectively activate tumor immunity, thereby enhancing the infiltration and activation of T cells, DCs, and macrophages. The dual degradation of β-catenin and STAT3 logically serves to counteract the TIME. The degradation of β-catenin aims to enhance the infiltration of the crucial DC cell subtype, $CD103^+$ DCs, which directly recruit $CD8^+$ T cells, creating an environment at both the cellular and molecular levels for T cells to exert anti-tumor cytotoxicity. On the other hand, the degradation of STAT3 directly activates multiple cellular processes in T cells. It stimulates their proliferation and maturation, promoting the recognition and killing of tumor cells by T cells. Notably, compared with the single-target degradation group, the dual-target degradation group showed significantly enhanced activation of $CD8^+$ T-cell cytotoxicity along with pronounced inhibition of M2-type macrophages. These findings suggested a synergistic effect associated with dual-target degradation in activating tumor immunity.

Furthermore, consistent with previous observations at the cellular level, the antitumor efficacy of NP-PROTACs in PDO and PDX models provided preliminary evidence supporting their promising clinical prospects.

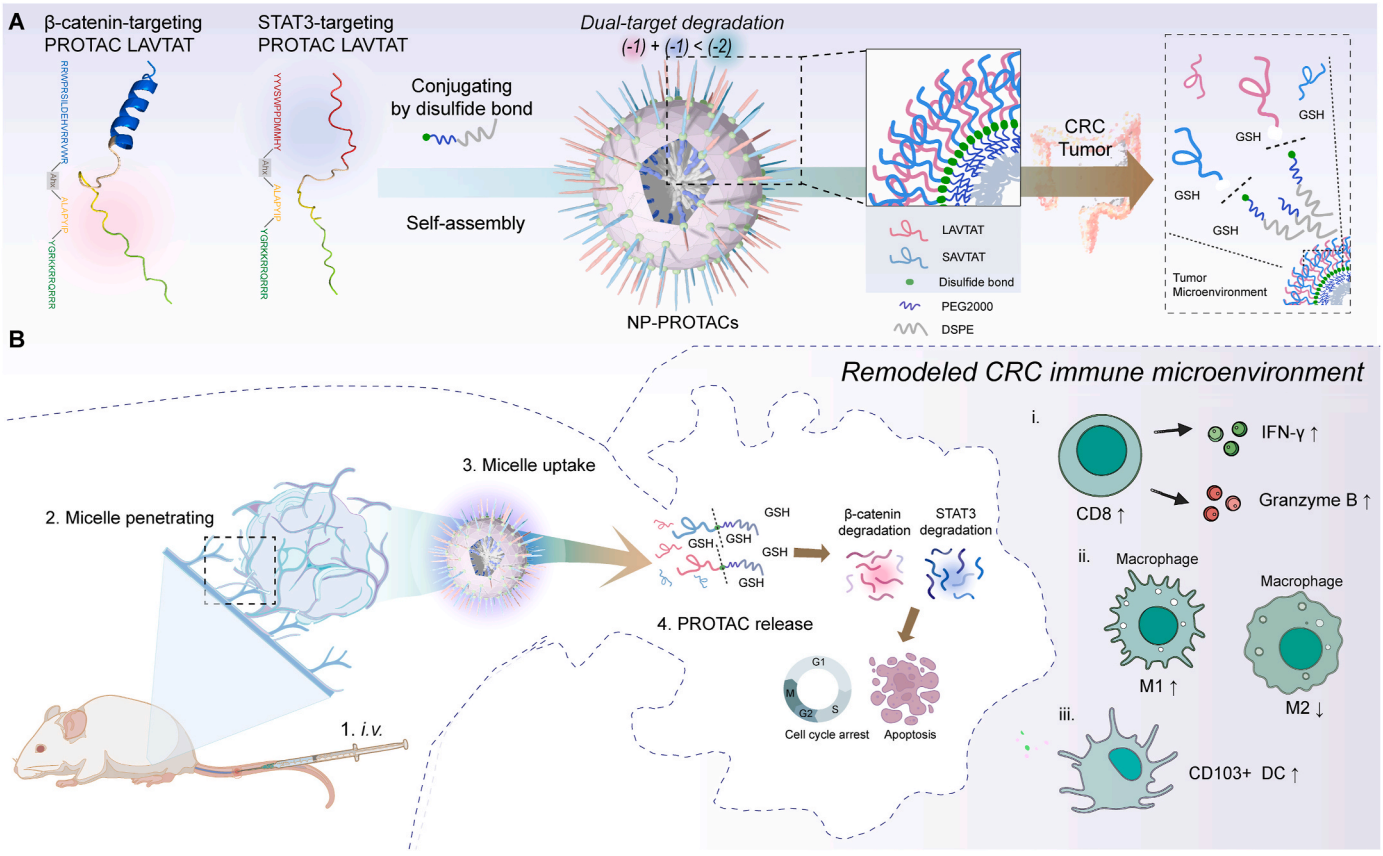

Fig. 9. Schematic diagram of the anti-tumor mechanism of dual-target-degrading NP-PROTACs. (**A**) β-catenin-targeting LAVTAT and STAT3-targeting SAVTAT were conjugated with DSPE-PEG_{2000}-SH through disulfide bonds, jointly self-assembling into NP-PROTACs. (**B**) Upon intravenous injection and accumulation in CRC models, NP-PROTACs released LAVTAT and SAVTAT intracellularly due to cleaved disulfide bonds. Co-degradation of β-catenin and STAT3 triggered cell cycle arrest and apoptosis on CRC cells and improved immune microenvironment. Briefly, the cytotoxic function of $CD8^+$ T cells was activated; an increase in the ratio of M1-type macrophages and a decrease in the ratio of M2-type macrophages were observed; the infiltration of $CD103^+$ DC cells was increased.

4. Conclusion

In conclusion, we presented reduction-responsive nanoengineered PROTACs capable of simultaneously degrading β-catenin and STAT3. We demonstrated that the NP-PROTACs can achieve enhanced bioavailability, deep tumor penetration, and improved efficacy compared with their peptide counterparts or single-target degradation at equivalent dosages. The dual-target combination therapy effectively inhibited colorectal cancer growth by stimulating the antitumor immune response cascade in mice. Our findings highlight the potential of dual-target degradation micelles for clinical application.

5. Experimental section

5.1. Materials and reagents

All reagents and solvents were purchased from Adamas-beta, GL Biotech, Energy Chemical or Sinopharm Chemical Reagent Co. Ltd. Rink Amide resin (loading 0.34 mmol/g) was purchased from Tianjin Nankai Hecheng Science & Technology Co. Ltd. DSPE-PEG_{2000}-SH was supplied from Xi'an Ruixi Biotechnology Co. Ltd. Antibodies for STAT1 (ab109461, 1:1000), STAT2 (ab32367,1:1000), STAT4 (ab68156,1:1000), c-Myc (ab32072, 1:1000), Dishevelled2 (ab124933, 1:1000), TCF4 (ab217668, 1:1000), GSK3β (ab32391, 1:1000), Axin1 (ab233652, 1:1000), and ubiquitin (ab134953, 1:500) were obtained from Abcam. Antibodies for STAT5 (JJ08-78, 1:500) and STAT6 (SY13-09, 1:500) were obtained from Huabio. Antibodies for β-catenin (8480s, 1:1000), STAT3 (9139s, 1:1000), PD-L1(13684, 1:1000), cyclin D1 (55506, 1:1000), BCL-XL (2764, 1:1000), and Alexa Fluor 647 conjugate (4418.1:1000) were from Cell Signaling Technology. Antibodies for CD3 (553240), CD4 (2005302), IFN-γ (557649), CD11c (558079), MHCII (746086), F4/80 (565853), CD86 (553692) were from BD Biosciences. Antibodies for CD45 (103130) and CD206 (141720) were from Biolegend. Antibodies for Granzyme B (2338642) were from Invitrogen. The antibody for CD8a (10122-80-100) was from Biogems. Antibody for CD11c (32-0112-U100) was from TONBO. Annexin V-FITC apoptosis assay kit, Human IL-2 ELISA kit (abs510001), Human IFN-γ ELISA kit (Plus) (abs551105), and Human TNF-α ELISA kit (abs510006) were purchased from Absin. The cell cycle and apoptosis analysis kit were purchased from Beyotime, and a Neofect DNA transfection reagent (TF20121201) was provided by SBS Genetech. Recombinant human STAT3 protein (P40763) was obtained from Novoprotein. Recombinant Human Catenin beta-1(CSB-EP006169HUa0) was obtained from CUSABIO.

5.2. Bioinformatic analysis

STAT3 and β-catenin expression in CRC was first analyzed from data from the Cancer Proteome Atlas (https://bioinformatics.mdanderson.org/public-software/tcpa/). The original RNA-Seq data and clinical information across the COAD, GSE31905, GSE4107, GSE8671 and GSE17536 datasets were obtained from The Cancer Genome Atlas (TCGA) platform (https://cancergenome.nih.gov/), Genomic Data Commons (GDC) platform (https://portal.gdc.cancer.gov/), and GEO online database, respectively. Then, the mRNA expression levels were determined via R software (v3.5.1). Briefly, the differentially expressed genes (DEGs) were identified by the limma package. Then, the mRNA expression patterns of these DEGs were visualized with heatmaps, box plots, or violin plots using the heatmaps or the ggplot2 package. KEGG gene sets were obtained through the Kyoto Encyclopedia of Genes and Genomes (https://www.kegg.jp/) and KEGGREST packages. Correlation coefficients between genes were calculated and plotted through the corrplot package. Single-cell transcriptomic data were obtained and visualized by the Single Cell Portal (https://singlecell.broadinstitute.org/single_cell). Survival data were obtained and plotted by GEPIA (http://gepia2.cancer-pku.cn/#index) and cbioportal (https://www.cbioportal.org/).

5.3. Cell lines

HCT116, CT26, and NCM460 cells were purchased from the Cell Bank of the Shanghai Institute of Cell Biology, Chinese Academy of Sciences, and cultured in McCoy's 5A (Gibco, 16600082) and 1640 (Gibco, 2192717) medium, respectively, supplemented with 10 % fetal bovine serum (FBS, Gibco, 10091148) and 1 % penicillinstreptomycin (PS, HyClone, SV30010). Jurkat cells were purchased from Shanghai Zhong Qiao Xin Zhou Biotechnology Co. Ltd. and cultured in 1640 medium supplemented with 10 % FBS and 1 % PS. All cell lines used in the study were maintained in a humidified incubator (Thermo Fisher, USA) containing 5 % CO_2 at 37 °C.

5.4. Analytical methods

^{1}H NMR spectra were obtained on a Bruker Avance 500 MHz NMR Spectrometer (Germany). The chemical shifts of the protons were given on the δ scale, ppm, with tetramethyl silane serving as the internal standard. All NMR experiments were conducted at room temperature unless otherwise stated. Analytical HPLC was performed on an Agilent 1260 Infinity LC instrument using an analytical column (ZORBAX Eclipse XDB 80 Å C18, 4.6 × 150 mm, 3.5 μm particle size, flow rate 1.0 mL/min, r.t.). Analytical injections were monitored at 214 nm. All separations used a mobile phase of 0.1 % trifluoroacetic acid (TFA) (v/v) in water (solvent A) and 0.1 % TFA (v/v) in CH_3CN (solvent B), with a linear gradient of 5–65 % solvent B in 30 min at room temperature. Semipreparative HPLC was performed on a Waters Auto Purification System (USA) instrument using a semipreparative column (XBridge Prep C18, 19 × 250 mm, 10 μm particle size, flow rate 20 mL/min). Solution A was 0.1 % TFA in water, and solution B was 0.1 % TFA in CH_3CN. The gradient was a linear gradient of 20-20 % B over 5 min and then a linear gradient of 20–60 % B over 50 min. The peptides were dissolved in H_2O to a final concentration of 50 μM.

5.5. Synthesis of peptides

Peptide sequences are shown in Table S1. All peptides were synthesized by standard Fmoc solid-phase peptide synthesis (SPPS) on the Rink Amide resin (initial loading = 0.34 mmol/g). Briefly, 735 mg resin was swelled with dichloromethane (DCM) for 20 min, followed by washing with N, N-dimethylformamide (DMF) 3 times. Fmoc deprotection of the resin was performed using 20 % piperidine/DMF/0.1 M Oxyma pure twice (5 min × 2). For each step of amino acid coupling, the resin was coupled with amino acid (1 mmol), N, N′-diisopropylcarbodiimide (DIC, 1 mmol), and Oxyma pure (1 mmol) in N-methyl-2-pyrrolidone (NMP, 6 mL) solvent. The reaction was conducted in a constant shaker for 20 min at 60 °C. Then, the resin was washed with DMF (3 times), DCM (3 times), and DMF (3 times), respectively. The deprotection, washing, coupling, and washing steps were assembled until all the amino acid residues were assembled. After washing the resin, it was treated with a 6 mL solution of acetic anhydride and pyridine (1:1) for 20 min. After the resin was washed with DMF (5 times) and DCM (5 times), a cocktail TFA solution (88 % TFA, 2 % triisopropylsilane, 5 % phenol. and 5 % water) was added to cleave the peptides from the resins for 2 h at room temperature. Then, the TFA was evaporated by blowing with N_2. The crude peptides were obtained by precipitation with 40 mL cold diethyl ether and centrifugation at 4000 rpm for 3 min (3 times). Finally, the crude products were allowed to air dry and purified by reversed-phase high-performance liquid chromatography (RP-HPLC) to obtain the final products. All peptides were confirmed by mass spectrum (MS) and possessed a purity of at least 95 % (Fig. S3).

5.6. Synthesis and characterization of micelles

Peptides with additional Cys residues at the N-terminus and 2,2′-dithiodipyridine were dissolved in methanol (MeOH) and stirred at room temperature for 24 h. The products were subsequently isolated in a dialysis bag (1000 Da, 45 mm, Spectrumlabs) in MeOH for 24 h, after which the dialysate was changed every 8 h. The pure powders were acquired after freeze-drying. Then, the pyridyl dithiol-terminated peptides and DSPE-PEG_{2000}-SH were dissolved in MeOH at a molar ratio of 1:5 and were placed in a dialysis bag (1000 Da, 45 mm, Spectrumlabs) at room temperature in MeOH for 24 h. Pure powders were acquired after freeze-drying. Two types of peptide-S-S-PEG_{2000}-DSPE (molar ratio = 1:1) were dissolved in chloroform: methanol (3:1) mixture and transferred in a round bottom flask. A dry film was generated by removing the organic solvent using a rotary evaporator under vacuum at 55 °C for 1 h. Then, 1 mL double-distilled water was added to hydrate the film at 55 °C and 200 rpm for 30 min. The products were confirmed by ^{1}H nuclear magnetic resonance (^{1}H NMR) spectroscopy. Micelles' particle size and zeta potential were measured by a Zetasizer Nano ZS instrument (Malvern, UK). The micelle morphology was characterized by TEM (JEM-1400 Plus, JEOL, Japan). The concentration of peptides in the micelle material was determined by HPLC with a standard curve. The synthesis of materials for self-assembled NP-PROTACs was confirmed by HPLC, ESI-MS, and ^{1}H NMR (Fig. S10 and 11).

5.7. Fluorescent labeling of peptides and micelles

ICG-DBCO, Cy5.5-DBCO, and DiR, purchased from Xi'an Ruixi Biological Technology Co. Ltd., were dissolved in DMSO at a 5 mg/mL concentration. LAVTAT-S-S-PEG_{2000}-DSPE, LAVTAT-S-S-PEG_{2000}-DSPE, LAVTAT, and SAVTAT with an additional Lys (N_3)-residue at the N-terminus were dissolved in the MeOH at a concentration of 1 mg/mL. The ICG-DBCO was reacted with LAVTAT-S-S-PEG_{2000}-DSPE and LAVTAT, respectively, at a molar ratio of 2:1, and Cy5.5-DBCO was reacted with SAVTAT-S-S-PEG_{2000}-DSPE and SAVTAT, respectively, at a molar ratio of 2:1 by a copper-free click reaction at room temperature overnight. Then, the products were isolated in a dialysis bag (2000 Da, 45 mm, Spectrumlabs) in MeOH for 24 h. Pure powders were obtained after freeze-drying. To prepare the DiR@NP-PROTACs, DiR and two types of peptide-S-S-PEG2000-DSPE (molar ratio = 1:1) were dissolved in chloroform: methanol (3:1) mixture and transferred in a round bottom flask. The subsequent steps were the same as described above.

5.8. Cell viability assay

Cell viability was examined using a Cell Counting Kit-8 (CCK-8, Meilunbio, MA0218). Cells were seeded into 96-well plates at a density of 5×10^3 cells/well and incubated overnight. Various concentrations of the peptides and micelles were dispersed in the culture medium with a serum concentration of 2.5 % and added for 24 h. Then, the medium was replaced with fresh serum-free medium containing 10 % CCK-8 solution, and the cells were incubated for another 2 h at 37 °C. The absorbance was detected by a Cytation 5 (BioTek, USA) microplate reader at 450 nm, and the half maximal inhibitory concentration (IC_{50}) was calculated by GraphPad Prism 8.

5.9. Cell cycle analysis

HCT116 cells (9×10^5 cells/well) were seeded into 6-well plates (3516, Corning) and treated with various concentrations of peptides. The cells were then washed twice with ice-cold 1 × PBS. After digestion, the cells were obtained and fixed in 70 % ethanol overnight at 4 °C. Finally, the cells were stained with PI plus RNase A (PI: RNase A = 1:9) for 1 h at room temperature and analyzed by flow cytometry.

5.10. Annexin V apoptosis assay

An Annexin V–FITC apoptosis assay kit (MA0220, Meilunbio) was used for cell apoptosis detection. HCT116 cells (9×10^5 cells/well) were seeded into 6-well plates (3516, Corning) and treated with various concentrations of peptides. After being washed with ice-cold PBS, the cells were obtained and fixed in binding buffer and 5 μL Annexin V-FITC for 15 min at room temperature. Then, PI reagent (5 μL) was added, and the cells were analyzed by flow cytometry.

5.11. Western blot assay

HCT116 cells (9×10^5 cells/well) or CT26 cells (5×10^5 cells/well) were grown in 6-well plates and exposed to peptides or micelles at various concentrations. Cells were lysed in ice-cold RIPA buffer (sc-24948, Santa Cruz Biotechnology Inc.) containing 50 protease inhibitors (catalog 11697498001). Total proteins were separated by 10 % (PG112) SDS-PAGE gel (EpiZyme) and transferred to a 0.2 μm PVDF membrane (10600021, Cytiva). The PVDF membranes were blocked in 1 × TBST (abs952, Absin) with 5 % nonfat milk for 1 h at room temperature. The signals were visualized by an Odyssey Infrared Imaging System (Tanon) and analyzed by using ImageJ software (NIH). β-Actin (ab6276, 1:1000) or GAPDH (ab8245, 1:1000) was used as a control.

5.12. Immunofluorescence

CT26 cells (5×10^5 cells/well) in a 20 mm confocal dish were treated with peptides for 9 h, fixed with 4 % paraformaldehyde for 20 min, and permeabilized with 0.5 % Triton X-100 (diluted with water) for 5 min. After blocking with 1 % BSA (MA0100, Meilunbio) in 1 × PBS (MA0015, Meilunbio) for 1 h at room temperature, the cells were stained with anti-STAT3 (1:1000, Cell Signaling Technology) and anti-β-catenin (1:1000, Cell Signaling Technology) at 4 °C overnight. Following incubation, the cells were washed with ice-cold 1 × PBS and incubated for another 60 min with a fluorescently labeled secondary antibody (1:500). The cells were washed with 1 × PBS and stained with Hoechst 33342 for 10 min. Fluorescence images were visualized using GE DeltaVision OMX SR.

5.13. Quantitative real-time RT-PCR (qRT-PCR)

Primers were shown in Table S3, and mouse GAPDH primers (B662304) were purchased from Sangon Biotech. Total RNA was extracted from cells using Trizol. Reverse transcription (RT) was performed with HiScript Q RT SuperMix for qPCR (Vazyme Biotech Co., Ltd., Nanjing, China). RT-PCR was performed in triplicate with a SYBR Green PCR Kit (Vazyme Biotech Co., Ltd., Nanjing, China) on an Applied Biosystems 7900HT sequence detection system (Applied Biosystems).

5.14. Separation of the Phases-based protein interaction Reporter (SPPIER)

Plasmids were shown in Table S2. HEK 293T cells were grown in 12-well plates at a density of 2×10^5 cells/well. The cells were cultured to approximately 70 % confluence and transfected with 1 μg of each plasmid DNA using Neofect DNA transfection reagent (TF20121201, Beijing Genomtech). Twenty-four hours after transient transfection, the cells were digested and seeded in confocal dishes (10^5 cells/well) overnight, and 10 μM peptides were added for 4 h. Fluorescence images were acquired using a GE DeltaVision OMX SR.

5.15. Hemolysis assay

The hemolytic activities of the peptides were evaluated by determining hemoglobin release from mouse blood suspensions. Fresh erythrocytes were obtained from whole blood by centrifuging at 4 °C and 1000×*g* for 30 min and washing with PBS 2 times. Then, the

erythrocytes were diluted with PBS at a volume ratio of 1:10. Then, 100 μL erythrocyte suspension was added to per well of a 96-well plate and incubated with peptides and conjugates solution at different concentrations for 1 h at 37 °C, followed by centrifugation at 1000 rpm for 10 min. The supernatants were obtained and monitored by measuring the absorbance at 570 nm (BioTek Cytation 5, USA). 0.1%Triton X-100 (v/v) was used as a positive control, and PBS was used as a negative control.

5.16. LDH release assay

A cytotoxicity lactate dehydrogenase release assay kit (DOJINDO, CK-12) was used to measure LDH release. CT26 cells were plated in triplicate wells in 96-well plates at a density of 5×10^3 cells/well. After culturing overnight, the medium in the wells was replaced with fresh medium containing SAVTAT for 4 h at different concentrations. Then, the medium in the wells was replaced with T cells (5×10^4 cells/well), and the cells were co-cultured for 24 h. For the positive control, T cells were replaced with fresh medium and lysis buffer for 30 min before the LDH test. After 24 h of incubation, the supernatant was aspirated from the 96-well plate and centrifuged to remove the suspended T cells, after which the LDH concentration was subsequently measured. Finally, the stop solution was added, and the absorbance was measured at 490 nm by a microplate reader (BioTek Cytation 5, USA).

5.17. In vitro binding assays by microscale thermophoresis (MST)

The binding affinity of the peptides to the STAT3 protein (Novoprotein) or β-catenin protein (CUSABIO) was determined by MST. Target proteins were labeled using the "Monolith NT.115TM protein Labeling Kit RED", which reacted efficiently with the primary amines of proteins to form highly stable dye-protein conjugates via N-hydroxysuccinimide (NHS)-ester chemistry. In the MST experiments, the concentration of the target proteins was kept constant while the peptides were serially diluted. The target proteins were mixed with 16 titration series of peptides at a volume ratio of 1:1. After a short incubation, the mixture was loaded into MST NT.115 standard glass capillaries and measured by Monolith NT.115 (NanoTemper, Germany).

5.18. Nanoparticle tracking analysis of NP-PROTACs

To analyze the reduction response of NP-PROTACs, NP-PROTACs (total mass concentration of 1 mg/mL) were dissolved in PBS containing 5 mM DTT or PBS and shaken at 37 °C and 200 rpm for 3 h. After 3 h, the samples were diluted 10 times with double-distilled water, and the particle size distribution was analyzed using Nanosight NS300. Images were captured for 30 s in a single experiment.

5.19. Drug release of NP-PROTACs

In a 50 mL beaker, FITC- and rhodamine B-labeled NP-PROTACs were separately dissolved in PBS containing 5 mM DTT and PBS and subjected to light-shielded dialysis at 37 °C. Additionally, two sets of FITC- and rhodamine B-labeled NP-PROTACs were separately dissolved in PBS containing 5 mM DTT and PBS and placed in EP tubes at 37 °C. At 1, 3, 6, 9, and 24 h, samples were taken from the dialysis bag (7000 Da, 45 mm, Spectrumlabs) or EP tubes, and the total volume in the dialysis bag and the fluorescence intensity were measured using a microplate reader (BioTek Cytation 5, USA). The fluorescence intensity in the liquid from the EP tubes at each time point was set as 100 %, and the drug release rate was calculated accordingly.

5.20. Cell uptake

For cell image acquisition, HCT116 cells were seeded (10^5 cells/dish) in confocal dishes overnight and treated with FITC-labeled LAVTAT, rhodamine B-labeled SAVTAT or NP-PROTACs (5 μM) for 2 h. Then, the cells were washed with cold PBS 3 times and stained with Hoechst 33342 to label the cell nuclei. Cell uptake was observed by a GE DeltaVision OMX SR (GE, USA). For flow cytometry analysis, HCT116 cells were seeded (9×10^5 cells/well) in 6-well plates overnight and treated with FITC-labeled LAVTAT, rhodamine B-labeled SAVTAT or NP-PROTACs (5 μM) for 0.5, 1, 2, or 4 h. The cells were digested and analyzed by flow cytometry.

5.21. Observation of the effect of SAVTAT using NanoLive 3D cell explorer

Cells were seeded in glass-bottom dishes at a density of 5×10^4 cells/well, incubated overnight, treated with 10 μM SAVTAT for 4 h, and then co-cultured with Jurkat cells (3×10^5 cells/well). The brightfield of the NanoLive 3D Cell Explorer was used to investigate the dynamic changes of cells.

5.22. Cell co-culture model

Before co-culturing with HCT116 cells, Jurkat cells were suspended in 1640 medium supplemented with 10 μg/mL PHA plus 10 ng/mL PMA to 10^6 cells/mL for 4 h. HCT116 cells were seeded in 12-well plates (1.5×10^5 cells/well) overnight, and treated with SAVTAT for 4 h. Then, the activated Jurkat cells were co-cultured with HCT116 cells for 48 h at a ratio of 1:6. The underlying living HCT116 cells were visualized with crystal violet staining. After being dissolved in 10 % acetic acid, the cells were quantified using a Cytation 5 microplate reader (BioTek) at 595 nm. Jurkat cells were stained with granzyme B, and analyzed by cell cytometry. The supernatant was collected, and the concentrations of IL-2 and TNF-α were determined via ELISA kits.

5.23. Spleen lymphocyte extraction and activation of T cells

The anti-mouse CD3e antibody was diluted to a concentration of 5 μg/mL in PBS. The diluted antibody was added to a 24-well plate (400 μL per well) and incubated at 4 °C overnight for coating. Spleen lymphocytes were isolated from the spleens of 6-week-old BALB/c mice via lymphocyte density gradient centrifugation according to Ficoll-Paque PREMIUM (Cytiva, 17544602) and subsequently cultured with 5 μg/mL anti-mouse CD28 antibody for 24 h. The activated spleen lymphocytes were subsequently cultured.

5.24. Co-incubation of T cells and CT26 cells

CT26 cells were seeded in 12-well plates (2×10^5 cells/well) overnight, treated with SAVTAT for 4 h, and co-incubated with activated spleen lymphocytes at a ratio of 1:10 for 24 h. Then, the spleen lymphocytes were collected and centrifuged at 500×*g* for 5 min at 4 °C. The supernatant was collected, and the concentrations of IFN-γ were determined via ELISA kits. T cells were stained with CD3, CD8a, CD4, and Granzyme B antibodies according to the instructions for flow cytometry. The underlying living CT26 cells were visualized via crystal violet staining. After being dissolved in 10 % acetic acid, the cells were quantified using a Cytation 5 microplate reader (BioTek) at 595 nm.

5.25. Flow cytometry analysis of T-cell proliferation

Before co-incubation with CT26, activated T cells were incubated with 10 μM 5-(and-6)-carboxyfluorescein diacetate succinimidyl ester (CFSE, Molecular Probes, Eugene, OR) dye in serum-free RPMI-1640 medium at 37 °C for 15 min. The T cells were then resuspended in a culture medium containing 10 % serum and co-incubation with CT26. After co-incubation, the fluorescence intensities of the CFSE-labeled T cells were analyzed by flow cytometry.

5.26. $CD103^+$ DC extraction and induction

Bone marrow-derived dendritic cells (BMDCs) were isolated from 6-week-old C57 female mice. Briefly, the tibias and femurs of mice were collected in a sterile environment, and the bone marrow cells were flushed with 1640 medium. The suspension was filtered through a 200-mesh nylon sieve mesh to remove the tissues and fragments. The red blood cells were separated with the red blood cell lysis buffer. After centrifugation at 1200 rpm for 5 min, the monocytes were washed and counted. $CD103^+$ DCs were induced according to previously reported methods [43]. BDMCs were suspended in 10 ng/mL GM-CSF and 200 ng/mL FLT3L to a concentration of 5×10^5/mL and were cultured in 100 mm dishes. On days 4 and 7, 5 mL of fresh medium supplemented with 10 ng/mL GM-CSF and 200 ng/mL FLT3L was added to each dish. On day 10, the loosely adherent cells were detached, resuspended in a fresh medium containing 10 ng/mL GM-CSF and 200 ng/mL FLT3L, and seeded into new dishes at the original density. On day 15, the cells were activated by adding 1 μg/mL LPS; after 24 h, $CD103^+$ DCs were stained with CD11c, MHCII, and CD103 for identification.

5.27. Transwell migration assay of $CD103^+$ DCs

Inserts from 24-well transwell plates (Costar, Sigma-Aldrich) were seeded with 2×10^6 $CD103^+$ DCs on the upper side of the transwell membrane, and 600 μL 1640 medium was added to the lower chamber of the transwell plate. After the cells and membrane were infused for 1.5 h, the lower chamber was exchanged with 500 μL HCT116 cell supernatant that had been treated with SAVTAT for 4 h. After 4 h, the $CD103^+$ DCs on the transwell membrane were stained with crystal violet.

5.28. Biodistribution

Five-week-old female BALB/c mice purchased from Shanghai Model Organisms Center Inc. were injected with 1×10^6 CT26 cells subcutaneously into the left axillary region. When the tumor volume reached approximately 200 mm^3, three mice from each group were injected via the tail vein with 100 μL (0.25 mg/kg ICG and 0.25 mg/kg Cy5.5) of free fluorescently-labeled PROTACs or fluorescently-labeled micelles. After 1, 3, 6, 9, 12, and 24 h, the mice were anesthetized and imaged under a Bio-Imaging Technology system (VISQUE In Vivo Elite) using a near-infrared fluorescence imaging system for ICG and Cy5.5 fluorescence distribution. Following *in vivo* imaging, the mice were sacrificed, and the tumors were harvested for ex vivo bioluminescence imaging. The results were analyzed using VISQUE Clevue software.

Five-week-old female BALB/c mice purchased from Shanghai Model Organisms Center Inc. were injected with 1×10^6 CT26 cells subcutaneously into the left axillary region. When the tumor volume reached approximately 200 mm^3, three mice from each group (free DiR or DiR@NP-PROTACs) were injected via the tail vein with 100 μL (0.2 mg/kg DiR) of free DiR or DiR@NP-PROTACs. After 24 h, the mice were sacrificed, and the major organs (heart, liver, spleen, lung, and kidney) and tumor were harvested for ex vivo bioluminescence imaging. The results were analyzed using VISQUE Clevue software.

5.29. In vivo antitumor therapy

Four-week-old female BALB/c mice were purchased from Shanghai Model Organisms Center, Inc., and kept under SPF conditions. The animal experiments were approved by the Committee on the Ethics of Animal Experiments of the Shanghai Model Organisms Center, Inc. A total of 5×10^5 CT26 cells suspended in 100 μL PBS were subcutaneously inoculated into the left axilla of the mice. The tumor volume was monitored periodically by a vernier caliper and calculated using the formula: volume (mm^3) = (length × $width^2$)/2, where length is the largest tumor diameter and width is the minor tumor diameter. When the average tumor volume reached about 50 mm^3, the mice were randomly divided into 4 groups (n = 6) and intravenously injected with PBS, NP-L, NP-S micelles, or NP-PROTACs. All formulations were administered every day for a total of 12 times. At the end of the experiment, the animals were sacrificed, and the tumors were collected for further study. The tumors were stained for H&E, Ki-67, TUNEL, STAT3, and β-catenin detection. H&E staining of major organs (heart, liver, spleen, lung, and kidney) was used to prove the safety of NP-PROTACs.

5.30. Analyses of the immune cell populations in tumors

Tumor tissues were made into single-cell suspensions, and the tumor-infiltrating lymphocytes were quantitatively analyzed by flow cytometry after immunofluorescence staining. In brief, tumor tissues were harvested and digested with a Tumor Dissociation Kit (Miltenyi Biotec, 130-096-730). For analysis of T cells, the cells were stained with CD45, CD3, CD4, CD8a, Granzyme B, and IFN-γ antibodies for flow cytometric analyses. For analysis of DCs, the cells were stained with CD45, CD11c, MHCII, and CD103 antibodies for flow cytometric analyses. For analysis of macrophages, the cells were stained with CD45, CD11b, F4/80, CD86, and CD206 antibodies for flow cytometric analyses.

5.31. PDO models of CRC

Organoids were established as described previously by D1Med Technology Inc. In this study, 50 organoids/well were seeded into 48-well plates and incubated in 5 % CO_2/95 % air at 37 °C for 6 days. The organoids were stained with fluorescence and photographed under a microscope (Zeiss, Vert A1), and the area of the live organoids was counted. On day 3, freshly prepared drug and medium mixtures were added. At the end of the sixth day, live/dead organoids were stained with fluorescence, and the area of live organoids (shown in green fluorescence) was photographed. The organoid survival rate was calculated by recording the organoid size (%) at specified concentrations. The formula is as follows: organoid survival rate = (organoids alive on day 6 in the NP-PROTACs group/organoid alive on day 0 in NP-PROTACs group)/(organoids alive on day 6 in the control group/organoids alive on day 0 in the control group) × 100 %.

5.32. PDX models of CRC

PDX models were constructed by Nanchang Royo Biotech Co., Ltd (Jiangxi, China). As the PDX volume reached approximately 100 mm^3, the mice were randomly divided into 2 groups and intravenously administrated with PBS or NP-PROTACs (10 mg/kg/day). The tumor volume and body weight were monitored every day.

5.33. Statistical analysis

GraphPad Prism 8.0.1 statistical analysis software (La Jolla, CA, USA) was used to analyze the data. The data were expressed as the mean ± standard deviation (SD) from at least three independent experiments. Student's t-test or two-way ANOVA, followed by Tukey's test, was applied for comparisons between two groups or among multiple groups, respectively: $^*P < 0.05$, $^{**}P < 0.01$, and $^{***}P < 0.001$. *n.s.* indicated no statistical significance.

Data availability

The data in this work are available in the manuscript or Supplementary Information, or available from the corresponding author upon reasonable request.

Ethics approval and consent to participate

The authors declare that they will follow the ethics for authorship,

review, and the authentic for the research and data.

Declaration of competing interest

The authors declare that they have no known competing financial interests or personal relationships that could have appeared to influence the work reported in this paper.

CRediT authorship contribution statement

Xinchen Lu: Writing – review & editing, Writing – original draft, Visualization, Methodology. **Jinmei Jin:** Writing – review & editing, Writing – original draft, Visualization, Methodology. **Ye Wu:** Writing – review & editing, Writing – original draft, Visualization, Methodology. **Jiayi Lin:** Writing – review & editing, Visualization. **Xiaokun Zhang:** Validation. **Shengxin Lu:** Validation. **Jiyuan Zhang:** Methodology. **Chunling Zhang:** Visualization. **Maomao Ren:** Writing – review & editing. **Hongzhuan Chen:** Supervision, Funding acquisition, Conceptualization. **Weidong Zhang:** Supervision, Conceptualization. **Xin Luan:** Supervision, Funding acquisition, Conceptualization.

Acknowledgments

This work was supported by National Natural Science Foundation of China, China (No. 82322073, 82173846, 82304790, 82304533), Oriental Scholars of Shanghai Universities, China (TP2022081), Jiangxi Province Thousand Talents Program, China (jxsq2023102168), Young Talent Lifting Project of China Association of Chinese Medicine, China [CACM-(2021-QNRC2-A08)], Shanghai Rising-Star Program, China (22QA1409100), 2021 Shanghai Science and Technology Innovation Action Plan, China (21S11902800), China Postdoctoral Innovative Talent Support Program, China (BX20220213), Shanghai Sailing Program, China (22YF1445000, 23YF1442600), Three-year Action Plan for Shanghai TCM Development and Inheritance Program, China [ZY (2021–2023)-0401; ZY (2021–2023)-0208], Organizational Key Research and Development Program of Shanghai University of Traditional Chinese Medicine, China (2023YZZ02), Innovation Team and Talents Cultivation Program of National Administration of Traditional Chinese Medicine, China (ZYYCXTD-D-202004), CAMS Innovation Fund for Medical Sciences (CIFMS), China (2023-I2M-3–009), Key project at central government level: The ability establishment of sustainable use for valuable Chinese medicine resources, China (2060302), High level Key Discipline of National Administration of Traditional Chinese Medicine, China (No. zyyzdxk-2023071), Innovation team of high-level local universities in Shanghai: Strategic Innovation Team of TCM Chemical Biology, China.

Appendix B. Supplementary data

Supplementary data to this article can be found online at https://doi.org/10.1016/j.bioactmat.2024.09.022.

References

[1] H. Sung, J. Ferlay, R.L. Siegel, M. Laversanne, I. Soerjomataram, A. Jemal, et al., Global cancer statistics 2020: GLOBOCAN estimates of incidence and mortality worldwide for 36 cancers in 185 countries, CA Cancer J. Clin. 71 (2021) 209–249, https://doi.org/10.3322/caac.21660.

[2] J. Kaellberg, A. Harrison, V. March, S. Berzina, I. Nemazanyy, O. Kepp, et al., Intratumor heterogeneity and cell secretome promote chemotherapy resistance and progression of colorectal cancer, Cell Death Dis. 14 (2023) 306, https://doi.org/10.1038/s41419-023-05806-z.

[3] U. Anand, A. Dey, A.K.S. Chandel, R. Sanyal, A. Mishra, D.K. Pandey, et al., Cancer chemotherapy and beyond: current status, drug candidates, associated risks and progress in targeted therapeutics, Genes Dis 10 (2023) 1367–1401, https://doi.org/10.1016/j.gendis.2022.02.007.

[4] H. Jin, L. Wang, R. Bernards, Rational combinations of targeted cancer therapies: background, advances and challenges, Nat. Rev. Drug Discov. 22 (2023) 213–234, https://doi.org/10.1038/s41573-022-00615-z.

[5] M.S. Hossain, H. Karuniawati, A.A. Jairoun, Z. Urbi, D.J. Ooi, A. John, et al., Colorectal cancer: a review of carcinogenesis, global epidemiology, current challenges, risk factors, preventive and treatment strategies, Cancers 14 (2022) 1732, https://doi.org/10.3390/cancers14071732.

[6] H. Zhao, T. Ming, S. Tang, S. Ren, H. Yang, M. Liu, et al., Wnt signaling in colorectal cancer: pathogenic role and therapeutic target, Mol. Cancer 21 (2022) 144, https://doi.org/10.1186/s12943-022-01616-7.

[7] X. Hu, J. Li, M. Fu, X. Zhao, W. Wang, The JAK/STAT signaling pathway: from bench to clinic, Signal. Transduct. Target Ther 6 (2021) 402, https://doi.org/10.1038/s41392-021-00791-1.

[8] J.X. Li, X.D. Ma, D. Chakravarti, S. Shalapour, R.A. DePinho, Genetic and biological hallmarks of colorectal cancer, Gene Dev. 35 (2021) 787–820, https://doi.org/10.1101/gad.348226.120.

[9] L. Nunes, F. Li, M. Wu, T. Luo, K. Hammarstrom, E. Torell, et al., Prognostic genome and transcriptome signatures in colorectal cancers, Nature (2024), https://doi.org/10.1038/s41586-024-07769-3.

[10] R. Zeng, H. Wu, X. Qiu, Z. Zhuo, W. Sha, H. Chen, Predicting survival and immune microenvironment in colorectal cancer: a STAT signaling-related signature, Qjm-Int. J. Med. 115 (2022) 596–604, https://doi.org/10.1093/qjmed/hcab334.

[11] Z.-H. Gao, C. Lu, M.-X. Wang, Y. Han, L.-J. Guo, Differential β-catenin expression levels are associated with morphological features and prognosis of colorectal cancer, Oncol. Lett. 8 (2014) 2069–2076, https://doi.org/10.3892/ol.2014.2433.

[12] M. Kawada, H. Seno, Y. Uenoyama, T. Sawabu, N. Kanda, H. Fukui, et al., Signal transducers and activators of transcription 3 activation is involved in nuclear accumulation of beta-catenin in colorectal cancer, Cancer Res. 66 (2006) 2913–2917, https://doi.org/10.1158/0008-5472.Can-05-3460.

[13] S. Zou, Q. Tong, B. Liu, W. Huang, Y. Tian, X. Fu, Targeting STAT3 in cancer immunotherapy, Mol. Cancer 19 (2020) 145, https://doi.org/10.1186/s12943-020-01258-7.

[14] M.J. Parsons, T. Tammela, L.E. Dow, WNT as a driver and dependency in cancer, Cancer Discov. 11 (2021) 2413–2429, https://doi.org/10.1158/2159-8290.Cd-21-0190.

[15] S. Spranger, R. Bao, T.F. Gajewski, Melanoma-intrinsic beta-catenin signalling prevents anti-tumour immunity, Nature 523 (2015) 231–235, https://doi.org/10.1038/nature14404.

[16] J.M. Jin, Y.P. Wu, Z. Zhao, Y. Wu, Y.D. Zhou, S.H. Liu, et al., Small-molecule PROTAC mediates targeted protein degradation to treat STAT3-dependent epithelial cancer, JCI Insight 7 (2022) e160606, https://doi.org/10.1172/jci.insight.160606.

[17] J.D. Beebe, J.Y. Liu, J.T. Zhang, Two decades of research in discovery of anticancer drugs targeting STAT3, how close are we? Pharmacol. Ther. 191 (2018) 74–91, https://doi.org/10.1016/j.pharmthera.2018.06.006.

[18] H. Zhang, C. Liu, D. Zhu, Q. Zhang, J. Li, Medicinal chemistry strategies for the development of inhibitors disrupting beta-catenin's interactions with its nuclear partners, J. Med. Chem. 66 (2023) 1–31, https://doi.org/10.1021/acs.jmedchem.2c01016.

[19] J. Lin, J. Jin, Y. Shen, L. Zhang, G. Gong, H. Bian, et al., Emerging protein degradation strategies: expanding the scope to extracellular and membrane proteins, Theranostics 11 (2021) 8337–8349, https://doi.org/10.7150/thno.62686.

[20] J.M. Jin, Y. Wu, J.J. Chen, Y.W. Shen, L.J. Zhang, H. Zhang, et al., The peptide PROTAC modality: a novel strategy for targeted protein ubiquitination, Theranostics 10 (2020) 10141–10153, https://doi.org/10.7150/thno.46985.

[21] M.J. Henley, A.N. Koehler, Advances in targeting 'undruggable' transcription factors with small molecules, Nat. Rev. Drug Discov. 20 (2021) 669–688, https://doi.org/10.1038/s41573-021-00199-0.

[22] I. Churcher, Protac-induced protein degradation in drug discovery: breaking the rules or just making new ones? J. Med. Chem. 61 (2018) 444–452, https://doi.org/10.1021/acs.jmedchem.7b01272.

[23] G. Posternak, X.J. Tang, P. Maisonneuve, T. Jin, H. Lavoie, S. Daou, et al., Functional characterization of a PROTAC directed against BRAF mutant V600E, Nat. Chem. Biol. 16 (2020) 1170–1178, https://doi.org/10.1038/s41589-020-0609-7.

[24] R.G. Guenette, S.W. Yang, J. Min, B. Pei, P.R. Potts, Target and tissue selectivity of PROTAC degraders, Chem. Soc. Rev. 51 (2022) 5740–5756, https://doi.org/10.1039/d2cs00200k.

[25] T.N. Grossmann, J.T.H. Yeh, B.R. Bowman, Q. Chu, R.E. Moellering, G.L. Verdine, Inhibition of oncogenic Wnt signaling through direct targeting of β-catenin, Proc. Natl. Acad. Sci. U. S. A. 109 (2012) 17942–17947, https://doi.org/10.1073/pnas.1208396109.

[26] N.D. Ambaye, H.E. Yu, Novel anti-cancer candidates from a combinatorial peptide library, Chem. Biol. Drug Des. 97 (2021) 87–96, https://doi.org/10.1111/cbdd.13763.

[27] H.W. Liao, X. Li, L.Z. Zhao, Y.L. Wang, X.D. Wang, Y. Wu, et al., A PROTAC peptide induces durable β-catenin degradation and suppresses Wnt-dependent intestinal cancer, Cell Discov 6 (2020) 35, https://doi.org/10.1038/s41421-020-0171-1.

[28] J. Han, H. Dong, T.Y. Zhu, Q. Wei, Y.H. Wang, Y. Wang, et al., Biochemical hallmarks-targeting antineoplastic nanotherapeutics, Bioact. Mater. 36 (2024) 427–454, https://doi.org/10.1016/j.bioactmat.2024.05.042.

[29] B.L. Wang, S.Q. Hu, Y. Teng, J.L. Chen, H.Y. Wang, Y.Z. Xu, et al., Current advance of nanotechnology in diagnosis and treatment for malignant tumors, Signal. Transduct. Tar. 9 (2024) 200, https://doi.org/10.1038/s41392-024-01889-y.

[30] F. Raza, H. Zafae, A.U. Khan, K.H. Kahkesh, T-cell membrane-coated nanomaterials in cancer treatment, Mat. Chem. Horizons 1 (2022) 199–217, https://doi.org/10.22128/MCH.2022.611.1028.

[31] X. Jin, G. Heidari, Z. Hua, Y. Lei, J. Huang, Z. Wu, et al., Nanoengineered polymers and other organic materials in lung cancer treatment: bridging the gap between research and clinical applications, EUR. Pol. J. 208 (2024) 112891, https://doi.org/10.1016/j.eurpolymj.2024.112891.

[32] J. Lopes, D. Lopes, A. Macario-Soares, I. Ferreira-Faria, D. Peixoto, M. Motallebi cell membrane-coated biomaterials for bone cancer-targeted diagnosis and therapy: a critical update on osteosarcoma applications, Mat. Chem. Horizons 2 (2023) 65–79, https://doi.org/10.22128/MCH.2022.615.1032.

[33] M. Green, M. Ishino, P.M. Loewenstein, Mutational analysis of HIV-1 Tat minimal domain peptides identification of trans-dominant mutants that suppress HIV-LTR-driven gene-expression, Cell 58 (1989) 215–223, https://doi.org/10.1016/0092-8674(89)90417-0.

[34] C.I. Chung, Q. Zhang, X. Shu, Dynamic imaging of small molecule induced protein-protein interactions in living cells with a fluorophore phase transition based approach, Anal. Chem. 90 (2018) 14287–14293, https://doi.org/10.1021/acs.analchem.8b03476.

[35] C.W. Chen, R.L. Huang, N. Wang, Y.F. Zheng, J.F. Zhou, B.W. Yang, et al., Fu-Zheng-Yi-Liu Formula inhibits the stem cells and metastasis of prostate cancer via tumor-associated macrophages/C-C motif chemokine ligand 5 pathway in tumor microenvironment, Chin. J. Nat. Med. 22 (2024) 501–514, https://doi.org/10.1016/S1875-5364(24)60653-9.

[36] G. Rizzo, A. Bertotti, S.M. Leto, S. Vetrano, Patient-derived tumor models: a more suitable tool for pre-clinical studies in colorectal cancer, J. Exp.Clin. Cancer Res. 40 (2021) 178, https://doi.org/10.1186/s13046-021-01970-2.

[37] F. Invrea, R. Rovito, E. Torchiaro, C. Petti, C. Isella, E. Medico, Patient-derived xenografts (PDXs) as model systems for human cancer, Curr. Opin. Biotech. 63 (2020) 151–156, https://doi.org/10.1016/j.copbio.2020.01.003.

[38] L. Shen, B. Wang, S.P. Wang, S.K. Ji, M.J. Fu, S.W. Wang, et al., Combination therapy and dual-target inhibitors based on LSD1: new emerging tools in cancer therapy, J. Med. Chem. 67 (2024) 922–951, https://doi.org/10.1021/acs.jmedchem.3c02133.

[39] M. Zheng, J. Huo, X. Gu, Y. Wang, C. Wu, Q. Zhang, et al., Rational design and synthesis of novel dual PROTACs for simultaneous degradation of EGFR and PARP, J. Med. Chem. 64 (2021) 7839–7852, https://doi.org/10.1021/acs.jmedchem.1c00649.

[40] Y. Shao, R. Su, Y. Wang, S. Yin, W. Pu, S. Koo, et al., Drug co-administration in the tumor immune microenvironment of Hepatocellular carcinoma, Acupunct. Herb. Med. 3 (2023) 189–199, https://doi.org/10.1097/HM9.0000000000000074.

[41] M. Chalabi, L.F. Fanchi, K.K. Dijkstra, J.G. Van den Berg, A.G. Aalbers, K. Sikorska, et al., Neoadjuvant immunotherapy leads to pathological responses in MMR-proficient and MMR-deficient early-stage colon cancers, Nat. Med. 26 (2020) 566–576, https://doi.org/10.1038/s41591-020-0805-8.

[42] M. Fakih, J. Sandhu, D. Lim, X. Li, S. Li, C. Wang, Regorafenib, Ipilimumab, and Nivolumab for patients with microsatellite stable colorectal cancer and disease progression with prior chemotherapy: a Phase 1 nonrandomized clinical trial, JAMA Oncol. 9 (2023) 627–634, https://doi.org/10.1001/jamaoncol.2022.7845.

[43] C.T. Mayer, P. Ghorbani, A. Nandan, M. Dudek, C. Arnold-Schrauf, C. Hesse, et al., Selective and efficient generation of functional Batf3-dependent CD103(+) dendritic cells from mouse bone marrow, Blood 124 (2014) 3081–3091, https://doi.org/10.1182/blood-2013-12-545772.